

Title	Intercomparison of NO <sub>3</sub> radical detection instruments in the atmosphere simulation chamber SAPHIR
Authors	Dorn, H. P.;Apodaca, R. L.;Ball, Stephen M.;Brauers, T.;Brown, Steven S.;Crowley, J. N.;Dubé, W. P.;Fuchs, H.;Häseler, R.;Heitmann, Uwe M.;Jones, R. L.;Kiendler-Scharr, Astrid;Labazan, I.;Langridge, J. M.;Meinen, J.;Mentel, T. F.;Platt, U.;Pöhler, D.;Rohrer, F.;Ruth, Albert A.;Schlosser, E.;Schuster, G.;Shillings, A. J. L.;Simpson, W. R.;Thieser, J.;Tillmann, R.;Varma, Ravi M.;Venables, Dean S.;Wahner, A.
Publication date	2013
Original Citation	Dorn, H.-P., Apodaca, R. L., Ball, S. M., Brauers, T., Brown, S. S., Crowley, J. N., Dubé, W. P., Fuchs, H., Häseler, R., Heitmann, U., Jones, R. L., Kiendler-Scharr, A., Labazan, I., Langridge, J. M., Meinen, J., Mentel, T. F., Platt, U., Pöhler, D., Rohrer, F., Ruth, A. A., Schlosser, E., Schuster, G., Shillings, A. J. L., Simpson, W. R., Thieser, J., Tillmann, R., Varma, R., Venables, D. S., and Wahner, A.: Intercomparison of NO <sub>3</sub> radical detection instruments in the atmosphere simulation chamber SAPHIR, Atmos. Meas. Tech. Discuss., 6, 303-379, doi:10.5194/amtd-6-303-2013, 2013
Type of publication	Article (non peer-reviewed)
Link to publisher's version	<a href="http://www.atmos-meas-tech-discuss.net/6/303/2013/">http://www.atmos-meas-tech-discuss.net/6/303/2013/</a> - 10.5194/amtd-6-303-2013
Rights	© Author(s) 2013. This work is distributed under the Creative Commons Attribution 3.0 License. - <a href="https://creativecommons.org/licenses/by/4.0/">https://creativecommons.org/licenses/by/4.0/</a>
Download date	2024-09-22 21:36:20
Item downloaded from	<a href="https://hdl.handle.net/10468/958">https://hdl.handle.net/10468/958</a>



# UCC

**University College Cork, Ireland**  
Coláiste na hOllscoile Corcaigh

Manuscript prepared for J. Name  
with version 4.2 of the L<sup>A</sup>T<sub>E</sub>X class copernicus.cls.  
Date: 5 December 2012

# **Intercomparison of NO<sub>3</sub> radical detection instruments in the atmosphere simulation chamber SAPHIR**

H.-P. Dorn<sup>1</sup>, R. L. Apodaca<sup>2</sup>, S. M. Ball<sup>3</sup>, T. Brauers<sup>1</sup>, S. S. Brown<sup>4</sup>,  
J. N. Crowley<sup>5</sup>, W. P. Dubé<sup>4</sup>, H. Fuchs<sup>4,1</sup>, R. Häsel<sup>1</sup>, U. Heitmann<sup>6</sup>, R. L. Jones<sup>7</sup>,  
A. Kiendler-Scharr<sup>1</sup>, I. Labazan<sup>5</sup>, J. M. Langridge<sup>7,11</sup>, J. Meinen<sup>8</sup>, T. F. Mentel<sup>1</sup>,  
U. Platt<sup>9</sup>, D. Pöhler<sup>9</sup>, F. Rohrer<sup>1</sup>, A. A. Ruth<sup>6</sup>, E. Schlosser<sup>1,12</sup>, G. Schuster<sup>5</sup>,  
A. J. L. Shillings<sup>7</sup>, W. R. Simpson<sup>2</sup>, J. Thieser<sup>9,13</sup>, R. Tillmann<sup>1</sup>, R. Varma<sup>6,14</sup>,  
D. S. Venables<sup>10</sup>, and A. Wahner<sup>1</sup>

<sup>1</sup>Institute of Energy and Climate Research, IEK-8: Troposphere, Forschungszentrum Jülich,  
Germany

<sup>2</sup>Department of Chemistry and Biochemistry and Geophysical Institute, University of Alaska,  
Fairbanks, AK, USA

<sup>3</sup>Department of Chemistry, University of Leicester, UK

<sup>4</sup>Earth System Research Laboratory, National Oceanic and Atmospheric Administration, Boulder,  
CO, USA

<sup>5</sup>Max-Planck-Institute for Chemistry, Mainz, Germany

<sup>6</sup>Physics Department & Environmental Research Institute, University College Cork, Cork, Ireland

<sup>7</sup>Department of Chemistry, University of Cambridge, UK

<sup>8</sup>Institute for Meteorology and Climate Research - Atmospheric Aerosol Research, Karlsruhe  
Institute of Technology, Germany

<sup>9</sup>Institute of Environmental Physics, University of Heidelberg, Germany

<sup>10</sup>Chemistry Department & Environmental Research Institute, University College Cork, Cork,  
Ireland

<sup>11</sup>now at: Earth System Research Laboratory, NOAA, Boulder, CO, USA

<sup>12</sup>now at: Institute for Meteorology and Climate Research, IMK-AAF, Karlsruhe Institute of  
Technology, Germany

<sup>13</sup>now at: Max-Planck-Institute for Chemistry, Mainz, Germany

<sup>14</sup>now at: Physics Department, National Institute of Technology Calicut, India

*Correspondence to:* H.-P. Dorn (h.p.dorn@fz-juelich.de)

**Abstract.** The detection of atmospheric  $\text{NO}_3$  radicals is still challenging owing to its low mixing ratios ( $\approx 1$  to 300 pptv) in the troposphere. While long-path differential optical absorption spectroscopy (DOAS) is a well established  $\text{NO}_3$  detection approach for over 25 years, newly sensitive techniques have been developed in the past decade. This publication outlines the results of the first  
5 comprehensive intercomparison of seven instruments developed for the spectroscopic detection of tropospheric  $\text{NO}_3$ . Four instruments were based on cavity ring-down spectroscopy (CRDS), two utilised open-path cavity enhanced absorption spectroscopy (CEAS), and one applied 'classical' long-path DOAS. The intercomparison campaign 'NO3Comp' was held at the atmosphere simulation chamber SAPHIR in Jülich (Germany) in June 2007. Twelve experiments were performed in  
10 the well mixed chamber for variable concentrations of  $\text{NO}_3$ ,  $\text{N}_2\text{O}_5$ ,  $\text{NO}_2$ , hydrocarbons, and water vapour, in the absence and in the presence of inorganic or organic aerosol. The overall precision of the cavity instruments varied between 0.5 and 5 pptv for integration times of 1 s to 5 min; that of the DOAS instrument was 9 pptv for an acquisition time of 1 min. The  $\text{NO}_3$  data of all instruments correlated excellently with the NOAA-CRDS instrument, which was selected as the common  
15 reference because of its superb sensitivity, high time resolution, and most comprehensive data coverage. The median of the coefficient of determination ( $r^2$ ) over all experiments of the campaign (60 correlations) is  $r^2 = 0.981$  (25th/75th percentiles: 0.949/0.994; min/max: 0.540/0.999). The linear regression analysis of the campaign data set yielded very small intercepts ( $1.2 \pm 5.3$  pptv) and the average slope of the regression lines was close to unity (1.02, min: 0.72, max: 1.36). The deviation of individual regression slopes from unity was always within the combined accuracies of each  
20 instrument pair. The very good correspondence between the  $\text{NO}_3$  measurements by all instruments for aerosol-free experiments indicates that the losses of  $\text{NO}_3$  in the inlet of the instruments were determined reliably by the participants for the corresponding conditions. In the presence of inorganic or organic aerosol, however, differences in the measured  $\text{NO}_3$  mixing ratios were detectable among  
25 the instruments. In individual experiments the discrepancies increased with time, pointing to additional  $\text{NO}_3$  radical losses by aerosol deposited onto the inlet walls of the instruments. Instruments using DOAS analyses showed no significant effect of aerosol on the detection of  $\text{NO}_3$ . No hint of a cross interference of  $\text{NO}_2$  was found. The effect of non-Lambert-Beer behaviour of water vapour absorption lines on the accuracy of the  $\text{NO}_3$  detection by broadband techniques was small and well  
30 controlled. The NO3Comp campaign demonstrated the high quality, reliability and robustness of performance of current state-of-the-art instrumentation for  $\text{NO}_3$  detection.

## 1 Introduction

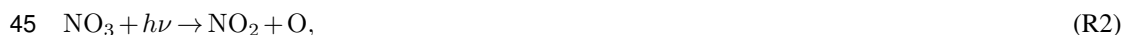
Radical chemistry in the polluted nighttime troposphere is governed by the abundance of  $\text{NO}_3$  radicals. They are very reactive and effectively oxidise alkenes, aldehydes, and biogenic volatile organic  
35 compounds (VOCs). Although their role as atmospheric oxidant during the day is negligible due to

their fast photolytic decomposition, their importance in atmospheric nighttime chemistry is comparable to that of OH radicals during daytime. Fundamental reviews on the physics and chemistry of NO<sub>3</sub> radicals were published by Wayne et al. (1991) and recently by Brown and Stutz (2012).

The key reactions controlling the nighttime formation and destruction of oxidised nitrogen are summarised in the following. In the troposphere NO<sub>3</sub> radicals are formed through the reaction of nitrogen dioxide with ozone.



During daytime NO<sub>3</sub> radicals do not build up to relevant levels (< 1 pptv) because they efficiently absorb light in the visible region of the solar spectrum leading to photolysis into a radical channel,



and a molecular channel



Based on these photolysis reactions the lifetime of NO<sub>3</sub> under typical daylight conditions is approximately 5 s. In addition NO<sub>3</sub> radicals react very rapidly with NO,



This reaction is important during the day, when its rate often exceeds that of photolysis, and in cases of fresh emissions of NO. At night the NO reaction often limits the lifetime of NO<sub>3</sub> when no excess O<sub>3</sub> is present to convert NO into NO<sub>2</sub>.

NO<sub>3</sub> itself reacts with NO<sub>2</sub> to form N<sub>2</sub>O<sub>5</sub> (the anhydride of nitric acid, HNO<sub>3</sub>),



N<sub>2</sub>O<sub>5</sub> is thermally unstable and can decompose into its precursors thereby establishing an equilibrium between NO<sub>3</sub> and N<sub>2</sub>O<sub>5</sub>. The back-reaction of (R5) is strongly temperature dependent, with N<sub>2</sub>O<sub>5</sub> being dominant at low temperatures. Recently Osthoff et al. (2007) remeasured the equilibrium constant of reaction (R5) to  $K_{eq}(T) = (5.1 \pm 0.8) \times 10^{-27} \exp((10871 \pm 46)/T) \text{ cm}^3 \text{ molecule}^{-1}$ . N<sub>2</sub>O<sub>5</sub> can efficiently be hydrolysed to HNO<sub>3</sub> on the surface of aerosol particles,



The wet and dry deposition of the HNO<sub>3</sub> formed by hydrolysis of N<sub>2</sub>O<sub>5</sub> is one of the most important loss reactions of oxidised nitrogen compounds in the atmosphere (Brown et al., 2006).

Owing to the high reactivity, the mixing ratio of NO<sub>3</sub> radicals in the troposphere is typically in the lower pptv range and their spatial and temporal variability can be high. This places high demands on the selectivity, sensitivity, and time resolution of measurement techniques used for NO<sub>3</sub> detection.

High quality, accurate, and precise in situ measurements of  $\text{NO}_3$  and  $\text{N}_2\text{O}_5$  are a prerequisite to understand the chemical processes controlling the chemistry of nocturnal nitrogen oxides and the significance of these species for the oxidising capacity of the nighttime troposphere. In the late 1970's the detection of  $\text{NO}_3$  radicals in the troposphere was pioneered by Platt and Perner (Platt and Perner, 1980; Platt et al., 1980). They used long-path Differential Optical Absorption Spectroscopy (DOAS) which evolved into a standard technique for the detection of atmospheric  $\text{NO}_3$ . DOAS has been widely used in different configurations in field experiments (e.g. Platt et al., 1981; Allan et al., 2000; Geyer et al., 2001, 2003; Stutz et al., 2004; McLaren et al., 2004; Sommariva et al., 2007; Vrekoussis et al., 2004, 2007) and chamber studies (e.g. Wängberg et al., 1997; Bossmeyer et al., 2006).

In the 1980s the Matrix-Isolation Electron Spin Resonance (MI-ESR) technique was developed, enabling absolute, calibration-free detection of  $\text{NO}_3$  radicals (Mihelcic et al., 1993). In a field inter-comparison on  $\text{NO}_3$  detection between DOAS and MI-ESR (Geyer et al., 1999), the latter worked very successfully. It however suffered from its inferior time resolution (sampling time  $\geq 30$  min) and substantial handling difficulties which only allowed a limited number of samples to be taken per day.

In the past 15 years new spectroscopic instruments for sensitive tropospheric  $\text{NO}_3$  detection have been developed. Their detection principle makes either use of the specific fluorescence properties of the  $\text{NO}_3$  molecule, as applied in Laser Induced Fluorescence (LIF) spectroscopy (Matsumoto et al., 2005; Wood et al., 2003), or takes advantage of its well resolved strong visible absorption band arising from the  $\tilde{B}^2E' \leftarrow \tilde{X}^2A'_2$  electronic transition on which the new cavity enhanced absorption techniques are based (cf. Ball and Jones, 2003; Brown, 2003, and references therein). Since the first laboratory detection of  $\text{NO}_3$  radicals by cavity ring-down spectroscopy (CRDS) by King et al. (2000), many cavity-based approaches have been developed (see, for instance, Ayers et al., 2005; Bitter et al., 2005; Brown et al., 2001, 2002a,b; Dubé et al., 2006; Fiedler et al., 2003, 2007; Simpson, 2003; Venables et al., 2006). Some of these instruments are also capable of measuring  $\text{N}_2\text{O}_5$  concentrations indirectly by quantitative thermal conversion into  $\text{NO}_3$  in a heated detection cell and the  $\text{N}_2\text{O}_5$  concentration is obtained after subtraction of the (generally much smaller)  $\text{NO}_3$  concentration. In this way, simultaneous measurements of  $\text{NO}_3$  and its equilibrium partner  $\text{N}_2\text{O}_5$  in the troposphere became feasible for the first time (Chang et al., 2011).

This publication presents the results of an intercomparison of instruments for the detection of tropospheric  $\text{NO}_3$  radicals that are all based on various absorption spectroscopic principles. The large atmosphere simulation chamber SAPHIR on the campus of Forschungszentrum Jülich was chosen for the 'NO3Comp' campaign where the instruments were able to be operated concurrently under controlled atmosphere-like conditions. Chamber experiments are more appropriate for inter-comparison exercises than field trials in the open atmosphere because natural spatial and temporal fluctuations of the air mass introduce additional variability and hence uncertainty to the measurement

105 conditions, which in turn causes the comparison data to be less reliable. The chamber, however, allows for controlled production of  $\text{NO}_3$  and  $\text{N}_2\text{O}_5$  from the reactions (R1) and (R5), and provides the opportunity for multiple instruments to sample from the same well-mixed volume of gas.

Each of the participating instruments adhered to a different calibration scheme and was likely to exhibit different sensitivity to potential artifacts such as reactive trace gases or aerosol. Hence the instruments were exposed to various representative atmospheric scenarios during twelve measurement days in June 2007. This activity was the first comprehensive multi-instrument intercomparison of  $\text{NO}_3$  detection instruments. Five of nine instruments participating in NO3Comp were also capable to detect  $\text{N}_2\text{O}_5$  and four instruments detected  $\text{NO}_2$  concurrently with  $\text{NO}_3$ . The results of the  $\text{NO}_2$  and  $\text{N}_2\text{O}_5$  measurements are reported in separate articles (Fuchs et al., 2010a, 2012). The ability of three broad-band instruments to quantify the extinction coefficient of aerosols during the campaign is described by Varma et al. (2012). All experiments during NO3Comp were conducted as an open instrument intercomparison where discussions between the participants were generally allowed.

## 2 Instrumental

### 2.1 Absorption cross section of $\text{NO}_3$

120 In the following sections the experimental setups of the seven  $\text{NO}_3$  detection instruments, as they were used at the SAPHIR chamber, are described in detail.

Since all instruments made use of absorption spectroscopy the participants of NO3Comp agreed before the campaign to apply the absorption cross section published by Yokelson et al. (1994) for the retrieval of the  $\text{NO}_3$  mixing ratio. Yokelson et al. measured the temperature dependence of the  $\text{NO}_3$  absorption cross section between 440–720 nm within the temperature range 200–298 K in laboratory experiments. The  $\text{NO}_3$  peak absorption cross section at 662 nm was reported to be  $(2.23 \pm 0.22) \times 10^{-17} \text{ cm}^2$  at 298 K ( $2\sigma$  error limits). With decreasing temperature this value was found to increase by 36 % at 200 K. Orphal et al. (2003) re-measured the visible  $\text{NO}_3$  spectrum using high-resolution Fourier transform spectroscopy ( $\Delta\lambda = 0.026 \text{ nm}$ ) and derived a parametrisation of the temperature dependence (200–330 K) of the peak cross section, which has been accepted into the current NASA/JPL recommendations (Sander et al., 2011). Excellent agreement exists between the Orphal model and the empirical relationships from Yokelson et al. (1994) and Osthoff et al. (2007). All groups participating in NO3Comp used this parametrisation to calculate the respective  $\text{NO}_3$  cross section valid for the specific temperature of their  $\text{NO}_3$  detection channel.

#### 135 2.1.1 Pulsed cavity ring-down spectrometer, NOAA-CRDS

The most mature instrument employed in this campaign was the NOAA (Boulder, CO, USA) pulsed cavity ring-down spectrometer measuring  $\text{NO}_2$ ,  $\text{NO}_3$ , and  $\text{N}_2\text{O}_5$  simultaneously in separate channels. At the time of the intercomparison, this instrument and its predecessors (Brown et al., 2001,

2002a,b) had already been deployed in a number of atmospheric field measurement campaigns on  
140 the ground (Brown et al., 2003, 2007), aboard an aircraft (Brown et al., 2005) and ships (Brown  
et al., 2004, 2005; Aldener et al., 2006).

The setup and performance of this instrument has been described in detail in the publication by  
Dubé et al. (2006). Inlet transmission and conversion efficiencies have been thoroughly studied  
by Fuchs et al. (2008). The NOAA-CRDS instrument consisted of 4 optical cavities used for the  
145 detection of  $\text{NO}_3$  and  $\text{N}_2\text{O}_5$  at 662 nm and two cavities (at 532 nm) were taken for calibration  
purposes and measurement of  $\text{NO}_2$  (Fuchs et al., 2010a). The temperature in the  $\text{NO}_3$  detection  
channel was actively controlled to match the outside temperature. A pulsed Nd:YAG pumped dye  
laser (repetition rate 50 Hz) provided light at 662 nm (FWHM  $\leq 1.5$  pm) to detect  $\text{NO}_3$ . In addition,  
about 5% of the light from the pump laser at 532 nm was used for the detection of  $\text{NO}_2$  (Fuchs et al.,  
150 2012). The 662 nm cavity mirrors were separated by 0.91 m and had a reflectivity of 99.999%. The  
light transmitted through the end mirror of the cavities was detected by photomultiplier tubes. The  
mixing ratio of the  $\text{NO}_3$  radicals was calculated from the difference between the ring-down times  
with ( $\tau$ ) and without ( $\tau_0$ )  $\text{NO}_3$  in the cavity and the  $\text{NO}_3$  absorption cross section ( $\sigma_{\text{NO}_3}$ ):

$$[\text{NO}_3] = \frac{R_L}{c\sigma_{\text{NO}_3}} \left( \frac{1}{\tau} - \frac{1}{\tau_0} \right) \quad (1)$$

155  $c$  is the speed of the light and  $R_L$  is the ratio of the physical cavity length to the length over which  
the absorber is present in the cavity. The latter was reduced because the volumes adjacent to the  
mirrors were purged with zero air in order to avoid contamination of the mirror surfaces. The value  
of  $R_L$  had been determined previously in laboratory experiments to be  $(1.15 \pm 0.03)$ . The zero ring-  
down time ( $\tau_0$ ) of the  $\text{NO}_3$  cavity was measured every 3 to 5 minutes by adding 40 ml of a mixture  
160 of 100 ppmv NO in nitrogen to the cavity for 5 s. This yielded an NO mixing ratio of 0.5 ppmv  
in the sampled air, which was enough to quantitatively titrate  $\text{NO}_3$  via reaction R4 before the gas  
entered the detection cavity. This method of determining the baseline signal allows to selectively  
separate the  $\text{NO}_3$  signal from the contributions of other atmospheric absorbers such as  $\text{NO}_2$ ,  $\text{O}_3$ ,  
and  $\text{H}_2\text{O}$ , and is superior to, e.g., flushing the cavity with zero air because it leaves the  $\text{O}_3$ , and water  
165 absorptions unchanged.

During  $\text{NO}_3\text{Comp}$  air was sampled from the chamber at a flow rate of 8 slm (standard litre per  
minute) through a Teflon-FEP line (i.d. 4 mm, total length about 0.4 m) extending about 0.2 m into  
the chamber. In order to minimise wall losses in the system the instrument operated at reduced  
pressure ( $\sim 350$  hPa). A Teflon filter (25  $\mu\text{m}$  thickness, 47 mm diameter, 2  $\mu\text{m}$  pore size) was placed  
170 downstream of the inlet to remove aerosol particles which scatter light efficiently and would there-  
fore constitute a large interference to a gas phase optical extinction measurement. Automated, reg-  
ular filter changes (0.5 h–3 h) ensured constant  $\text{NO}_3$  loss on the filter, which was well characterised  
when clean (Dubé et al., 2006; Fuchs et al., 2008).

The dye laser (tuning uncertainty  $\pm 0.02$  nm) was fine tuned to a point on the broad maximum of  
175 the  $\text{NO}_3$  absorption spectrum ( $\approx 661.94$  nm) that is not resonant with any of the discrete water vapor

absorption transitions in this region. The laser wavelength was not actively controlled but checked regularly by scanning across the water absorption lines around the  $\text{NO}_3$  absorption peak.

Ring-down times of all channels were determined every second from the sum of 50 ring-down transients. Mixing ratios were corrected for possible changes in the  $\text{NO}_2/\text{NO}_3/\text{N}_2\text{O}_5$  equilibrium (R5) due to temperature differences between the chamber and the ring-down detection cells. A model simulated the changes assuming a linear temperature profile between the measured SAPHIR temperature and the constant temperature in the cavity. The correction was typically  $<0.5\%$ , with maximal differences during the campaign of ca.  $5\%$  at high  $\text{NO}_2$  mixing ratios. Extinction corrections (typically  $<2\%$ ) were made for varying Rayleigh scattering losses as well as for  $\text{NO}_2$ , and  $\text{O}_3$  absorption (at 662 nm).

The accuracy of cavity ring-down data was dominated by the uncertainty of the absorption cross section ( $\pm 5\%$ ,  $1\sigma$ ), the error of the effective cavity length ( $\pm 3\%$ ), and the  $\text{NO}_3$  transmission efficiencies of the cavity and the inlet/filter assembly. Calibrations based on standard additions to the inlet were unreliable and were made infrequently during the campaign due to a contamination in the  $\text{N}_2\text{O}_5$  source used to generate  $\text{NO}_3$ . Therefore, laboratory measurements of the  $\text{NO}_3$  transmission reported by Fuchs et al. (2008) of  $92 \pm 3\%$  were used for evaluation of all data during the campaign. An additional  $10\%$  error was estimated in order to account for a possible systematic uncertainty of the  $\text{NO}_3$  transmission during the campaign. The overall accuracy for NO3Comp was therefore  $+17\% / -5\%$ . The precision was determined from repeated measurements of  $\tau_0$  in zero air at 1 s data acquisition (Dubé et al., 2006). Under field measurement conditions values between 0.2 pptv and 0.5 pptv were obtained.

### 2.1.2 Off-axis cavity ring-down spectrometer, UAF-CRDS

A prototype diode-laser pumped cavity ring-down instrument using off-axis excitation of the cavity (Paul et al., 2001; Kasyutich et al., 2002) was used by the group of the University of Alaska, Fairbanks (USA). The setup was mainly based on the same technical principles as described by Ayers et al. (2005). The emission intensity of a temperature stabilised diode laser (662 nm) was square-wave modulated (100% modulation depth) at a rate of 500 Hz and directed into an optical cavity consisting of two highly reflective mirrors ( $>0.99995$  at 662 nm) that were separated by 0.66 m. A purge flow (0.2 slm) of synthetic air protected the mirrors. Light transmitted through the second mirror was collected by an off-axis parabolic mirror and directed into a photomultiplier tube whose signal was digitised at a rate of 5 MS/s by a 12-bit ADC. Air was sampled from the chamber at 8 slm through a Teflon inlet line (length 0.4 m, i.d. 6.3 mm). To remove particulate matter the sample gas flowed through a Teflon filter (Pall Teflo,  $2\ \mu\text{m}$  pore size) which was changed daily at the beginning of each experiment. The residence time of the sample gas in the measurement cell was 2 s. The cell consisted entirely of PFA teflon tubing (i.d. 16 mm).

During NO3Comp it was noticed that the laser occasionally oscillated on two longitudinal modes

leading to multi-exponential ring-down decay. These events were diagnosed and the corresponding data was excluded from the analysis. All data were corrected for the effective length of the cavity. The transmission efficiency of  $\text{NO}_3$  was determined for each filter several times a day from measurements at different sample flow rates (i.e., for different residence times). An initial transmission of 76 % was found and a typical decay rate of -0.4 %/hour was inferred from the plot of transmission versus filter use time. Both values were applied for all measurements during NO3Comp. Possible re-equilibration between  $\text{NO}_3$  and  $\text{N}_2\text{O}_5$  due to different temperatures between SAPHIR chamber air and gas sample inside the detection cell was analysed using a simple equilibrium model. At low  $\text{NO}_2$  mixing ratios (< 20 ppbv) the correction factor was small and reached maximal values around 13 % per degree of temperature difference ( $\Delta T$  was always < 2 K) at high  $\text{NO}_2$  mixing ratios. The zero ring-down time  $\tau_0$  was determined regularly by addition of nitric oxide to the sample air resulting in an NO mixing ratio of 50 ppbv in the measurement cell. The NO also reacts with  $\text{O}_3$  forming  $\text{NO}_2$ . At 662 nm the  $\text{NO}_2$  absorption is 1.39 times stronger than that of  $\text{O}_3$  resulting in an offset of a few pptv  $\text{NO}_3$  equivalent at 100 ppbv  $\text{O}_3$ . Moreover it was noted, that the NO titrant cylinder was contaminated with traces of  $\text{NO}_2$ , so that adding NO also resulted in addition of some  $\text{NO}_2$  (<1 pptv  $\text{NO}_3$  equivalent). The  $\text{NO}_3$  mixing ratios were corrected for both interfering processes.

The instrument as operated during NO3Comp had a noise-equivalent  $1\sigma$ -detection limit of 0.5 pptv in 1 s. The total accuracy of the UAF-CRDS instrument was 20 % ( $1\sigma$ ) taking into account an uncertainty of 17 % in the transmission efficiency of the inlet and measurement cell, 5 % uncertainty in the peak cross section for  $\text{NO}_3$ , and 10 % uncertainty of the effective cavity length.

### 2.1.3 Cavity ring-down Spectrometer, MPI-CRDS

During the intercomparison campaign the cavity ring-down instrument from the Max-Planck Institute for Chemistry (Mainz, Germany) was employed for the first time outside the laboratory. The instrument could be operated either in cavity ring-down (CRDS) or in cavity enhanced absorption mode (CEAS) (Schuster et al., 2009). Although the CEAS mode had lower noise levels ( $\sim 0.2$  pptv in 1 s) baseline drifts limited the accuracy of this device and all data reported here were measured exclusively based on the CRDS principle. The emission of a pulsed laser diode emitting close to 662 nm (100 % square-wave power modulated at 200 Hz) entered the cavity off-axis (mirror reflectivity  $\approx 99.998$  %). The light exiting the cavity was detected by a photomultiplier (PMT) through a 590 nm cut off filter and a 662 nm interference filter. The photomultiplier signal was digitised with a 100 MHz, 9 bit oscilloscope and averaged resulting in a time resolution of 5 s. The mirror distance was 0.7 m, sheath flows of zero air protected the mirrors. The cavity enclosure was made from Pyrex glass (i.d. 15 mm), coated with a film of Teflon (DuPont FEP 121a).

Typical ring-down times were measured to be 86–100  $\mu\text{s}$ .  $\tau_0$  was recorded by adding NO upstream of the Teflon filter and complete titration of  $\text{NO}_3$  was established within 0.1 s. Usually one

minute of NO<sub>3</sub> measurement was followed by one minute of background measurement. The effect of adding NO to air samples containing O<sub>3</sub> on the total absorption at 662 nm was taken into account in the final analysis. Air was sampled from the SAPHIR chamber at a flow rate of 8 slm through a 0.68 m long PFA tubing (9.5 mm i.d.), protruding 0.39 m into the chamber. A 22 mm diameter Teflon membrane filter (pore size 2 μm) eliminated particles from the air stream. The average residence time within the optical cavity was ≈ 1 s.

Random fluctuations in the ring-down times resulted in an NO<sub>3</sub> precision (1σ-detection limit) of 3 pptv for a 10 s acquisition time. The accuracy of the measurement was governed by systematic errors in the absorption cross section of NO<sub>3</sub>, errors in the inlet gas transmission, correction for filter loss, and effective absorption path length. The NO<sub>3</sub> inlet losses were measured during four experiments at times of constant NO<sub>3</sub> in the chamber by variation of the flow rate through the instrument. An averaged correction factor of 1.13 ± 0.1 was applied. Filter losses were determined after the campaign in the lab and a correction factor of 1.18 ± 0.1 was determined. The overall 1σ accuracy of the NO<sub>3</sub> measurement by MPI-CRDS was estimated at about 14 %.

#### 2.1.4 Broadband cavity ring-down spectrometer, ULEIC-BBCRDS

The operating principles of the broadband cavity ring-down spectrometer of the University of Leicester (UK) have been discussed in Ball and Jones (2003, 2009), and an example of applying this instrument to measure ambient NO<sub>3</sub> during the NAMBLEX field campaign has been described by Bitter et al. (2005). The instrument's dye laser and CCD camera detector were upgraded following the NAMBLEX campaign; further details of the new hardware deployed for the SAPHIR intercomparison are given by Shillings et al. (2011).

A free running dye laser, pumped by a Q-switched Nd:YAG laser at 20 Hz repetition rate, was employed as the broadband light source. A mixture of DCM and LDS698 dyes dissolved in methanol/DMSO was used to obtain laser emission with an approximately Gaussian spectrum (16 nm FWHM centred at 662 nm). The ring-down cavity was mounted 0.3 m below the SAPHIR chamber, supported from the same optical table as the laser. The cavity mirrors (diameter 20 mm, separation 1.83 m, peak reflectivity 99.996 % at 680 nm) were held in adjustable bellows mounts attached to a thermally insulated Teflon tube (i.d. 19 mm) that formed the main body of the cavity. To reduce contamination of the mirror surfaces, the mirrors were purged with 0.5 slm of dry synthetic air. Hence the absorption measured over the full cavity length was multiplied by an experimentally determined length factor of  $R_L = 1.05$  to correct for the gas sample being excluded from regions immediately in front of the mirrors. Air was drawn from the SAPHIR chamber through four parallel Teflon tubes (i.d. 3 mm, length 0.4 m, tubes protected from sunlight outside the chamber); the tubes projected 15 cm above the chamber's floor to sample gas uncompromised by wall effects. The sample flow rate of 10.1 slm corresponded to a mean residence time of 2.7 s inside the cavity. Light exiting the ring-down cavity was collected by a lens and focused into a 200 μm diameter optical fibre

attached to an imaging Czerny-Turner type spectrograph ( $f = 250$  mm,  $f/4$  optics, spectral resolution  
285 0.36 nm FWHM). Time resolved spectra of light exiting the cavity were measured using a clocked  
CCD camera with an image sector of 512 pixels along the frame transfer axis (i.e., time) and 512 pixels  
along the wavelength dispersed axis (spectral coverage 645-683 nm, although in practice only the  
central 652-673 nm contributed usefully to the BBCRDS spectra recorded here). A slit-mask bonded  
to the CCD chip resulted in the cavity output illuminating only 5 pixels rows on the frame transfer  
290 axis. Thus the CCD's clocking rate of  $0.65 \mu\text{s}$  per pixel produced a minimum time resolution of  
 $3.3 \mu\text{s}$ .

Owing to its broadband detection approach, BBCRDS is sensitive to all molecules that contribute  
structured features to the measured absorption spectrum (Ball and Jones, 2003, 2009). The absolute  
concentrations of the relevant absorbers,  $n_i$ , ( $\text{NO}_3$ ,  $\text{NO}_2$ , and  $\text{H}_2\text{O}$ ) were obtained by fitting the  
295 measured absorption spectrum,  $\alpha(\lambda)$ , with a linear combination of reference cross sections of the  
trace gases,  $\alpha_i(\lambda)$ , convoluted with the spectral response function of the BBCRDS instrument. The  
sample's absorption spectrum was calculated from wavelength-resolved ring-down times measured  
when the cavity contained the sample,  $\tau(\lambda)$ , and when the cavity was purged with dry synthetic air,  
 $\tau_0(\lambda)$ .

$$300 \quad \alpha(\lambda) = \alpha_{bb}(\lambda) + \sum_i \sigma_i(\lambda) \cdot n_i = \frac{R_L}{c} \cdot \left[ \frac{1}{\tau(\lambda)} - \frac{1}{\tau_0(\lambda)} \right] \quad (2)$$

Because air drawn from the chamber was not filtered for aerosol, the broadband absorption back-  
ground due to aerosol scattering,  $\alpha_{bb}(\lambda)$ , was accounted for by a polynomial function of second or  
third degree. Ozone has a weak, but detectable, broadly-structured absorption at the wavelengths  
employed here; ozone was not included in the spectral fitting routine, instead its absorption was sub-  
305 tracted from the fitted  $\alpha_{bb}(\lambda)$  background using ozone concentrations measured by SAPHIR's core  
instruments.

Water vapor is the largest contributor to the differential structure in atmospheric spectra around  
662 nm, with line widths substantially narrower than the spectral resolution of the BBCRDS instru-  
ment leading to non-Lambert-Beer absorption behaviour. Slight errors in fitting the water absorption  
310 features have been shown to mask the  $\text{NO}_3$  absorption features and lead to spurious  $\text{NO}_3$  retrievals.  
The approach to quantitatively evaluate the water vapor concentrations from the measured multi-  
exponential decay of the cavity output has been described by Ball and Jones (2003, 2009), Bitter  
et al. (2005), Langridge et al. (2008a), and Shillings et al. (2011), and these methods were again  
applied to the present data set.

315 BBCRDS spectra were analysed assuming that the gas temperature inside the thermally insulated  
cavity was the same as inside SAPHIR. Consequently no corrections were made to the submitted  
data for  $\text{NO}_3/\text{N}_2\text{O}_5$  re-equilibration (reaction (R5)). In fact, temperature measurements taken in-  
frequently during the campaign showed the gas inside the cavity to be marginally cooler than inside  
SAPHIR. Box modelling performed post-campaign indicated that the mean  $\text{NO}_3$  mixing ratio inside

320 the cavity was 95.8 % of that in the SAPHIR chamber itself, assuming a representative 1.5 K temperature drop on entering the cavity and a 2.7 s residence time. Thus the BBRDS data are subject to a small, systematic under-measurement of the NO<sub>3</sub> mixing ratio by typically around 4 % due to NO<sub>3</sub> re-partitioning to N<sub>2</sub>O<sub>5</sub>. The model showed the worst under-measurement to be 9 % when gas inside SAPHIR was at its warmest.

325 A small amount of ambient air (< 6 % of the total flow) was found to be leaking into the BBRDS cavity during the campaign. The leak rate into the cavity was quantified for each experiment by comparing the measured water vapour mixing ratio in the cavity with data from a dew point hygrometer in the SAPHIR chamber. NO<sub>3</sub> mixing ratios reported were corrected for the dilution caused by this leak, and an overall uncertainty of 5 % for this effect was estimated. The leak was assumed not to  
330 contribute any additional chemical loss of NO<sub>3</sub>. The NO<sub>3</sub> loss rate on the walls and inlet of the instrument was measured during the campaign by varying the flow rate (i.e., residence time) of the sample through the BBRDS system. For the standard flow conditions (10.1 slm), the loss rate was  $k_w = 0.045 \text{ s}^{-1}$  corresponding to a NO<sub>3</sub> transmission efficiency of 0.75, and this value was applied to correct the whole BBRDS NO<sub>3</sub> data set. Whilst the uncertainty on this one measurement of  $k_w$   
335 was relatively small ( $\pm 3 \%$ ), it is likely that the NO<sub>3</sub> transmission losses varied somewhat throughout the campaign. In line with other instruments, conservatively, a  $\pm 10 \%$  error was assigned on the 0.75 efficiency used to correct for the instrument's inlet/wall losses.

The overall accuracy of the BBRDS NO<sub>3</sub> measurements is +15 % / -12 %, inferred from adding the individual sources of measurement error (length factor  $\pm 5 \%$ ; NO<sub>3</sub>/N<sub>2</sub>O<sub>5</sub> re-equilibration 0 to  
340 -9 %; air leak  $\pm 5 \%$ ; NO<sub>3</sub> wall loss  $\pm 10 \%$ ). The BBRDS accuracy becomes +16 % / -13 %, including the 5 % uncertainty in the NO<sub>3</sub> absorption cross section. The precision of the retrieval of the NO<sub>3</sub> mixing ratio (and other absorbers) was determined from the error of a linear fit to the absorber's absorption coefficients as a function of the corresponding absorption cross section. This method has been shown to produce robust estimates of the measurement precision and detection  
345 limits in other broadband cavity systems, e.g. Langridge et al. (2008b). The precision for the present NO<sub>3</sub> data set was typically 2 pptv ( $1\sigma$ ) for the 61 s averaging time.

### 2.1.5 Incoherent-broadband cavity enhanced absorption spectrometer, UCC-IBBCEAS

The IBB-CEAS instrument of University College Cork (Cork, Ireland) is a broadband multi-component absorption technique using an optical cavity to measure the total extinction of an air  
350 sample (Fiedler et al., 2003). Instead of observing the temporal decay of the light intensity inside the cavity as in CRDS, the steady state intensity  $I$  of light leaking out of the cavity is measured spectrally resolved. Setup and characteristics of the UCC-IBBCEAS instrument used during the campaign, and details of the data evaluation procedure have been published by Varma et al. (2009). The underlying theory of cavity enhanced absorption spectroscopy has been described in Fiedler  
355 et al. (2003, 2005, 2007); Venables et al. (2006); Gherman et al. (2008), and Triki et al. (2008).

The instrument consisted of a transmitter unit and a receiver unit, each housing one of the cavity mirrors (radius of curvature 21 m, diameter 4 cm, nominal reflectivity 0.9987 at 660 nm). The units were installed at the North and South ends of the SAPHIR chamber resulting in a geometrical mirror distance of the open-path CEAS cavity of  $20.13 \pm 0.05$  m. Considering the length of the cavity the setup was very stable. The cavity mirrors needed only marginal realignment during the campaign. The transmitter unit housed a 300 W 'hot-spot' Xe lamp. The light was imaged onto an iris using two off-axis parabolic mirrors. Between the mirrors the wavelength range was selected with a dielectric band-pass filter (610–720 nm). Because the light spot tended to wander on the cathode a fraction of the light was focused onto a quadrant detector which triggered a feedback loop to correct for changes in spot position. A telescope imaged the iris aperture approximately into the centre of the open-path cavity. Light transmitted by the cavity was further filtered in the receiver unit with a long-pass cut-off filter (Schott RG630) and a 700 nm short-pass interference filter to ensure that light outside the mirror reflectivity range was eliminated. The light was focused into a fibre bundle (1 mm diameter) and connected to the 100  $\mu\text{m}$  entrance slit of a spectrometer ( $f = 0.33\text{m}$ , spectral resolution 0.6 nm). A spectral interval from 620 nm to 720 nm was detected by a CCD detector and an acquisition time of 5 s was used for all  $\text{NO}_3$  measurements.

The transmitter and receiver units were each equipped with a 1 m stainless steel pipe (diameter 57 mm) pointing from the cavity mirrors along the optical axis of the cavity. A seal was made between the pipes and the adjustable mirror mounts of the cavity mirrors using flexible Teflon foil in each unit. The pipes served three purposes: Firstly, they allowed the mirrors to be purged with pure nitrogen with a flow rate of 10 slm which caused the effective cavity length to be  $L_{eff} = 18.27 \pm 0.20$  m. Secondly, on the receiver side of the setup the pipe reduced stray light entering the detection system. Thirdly, the pipes were necessary to install the instrument to the outside of the SAPHIR chamber and to make a seal with its teflon wall.

The total extinction,  $\alpha(\lambda)$ , of the air sample is calculated by:

$$\alpha(\lambda) = \frac{1 - R(\lambda)}{L_{eff}} \left( \frac{I_0(\lambda)}{I(\lambda)} - 1 \right) \quad (3)$$

where  $I_0(\lambda)$  and  $I(\lambda)$  are the intensities transmitted by the cavity in zero air and with a sample gas, respectively,  $R(\lambda)$  is the average mirror reflectivity, and  $L_{eff}$  is the effective cavity length (Fiedler et al., 2003). The UCC-IBBCEAS instrument used an open cavity, hence, the background intensity  $I_0(\lambda)$  in zero air could only be determined once a day in the morning after the chamber was flushed over night and before trace gases were introduced into the chamber.

To provide absolute absorption measurements using the IBB-CEAS principle, the reflectivity of the cavity mirrors  $R(\lambda)$  has to be known across the bandwidth of the measurement. During  $\text{NO}_3\text{Comp}$   $R(\lambda)$  was measured daily by moving an antireflection coated window of well known loss into the cavity in zero air (Varma et al., 2009). The total loss (reflection plus transmission) of the window was determined in the lab with a pulsed cavity ring-down instrument as a function of wavelength ranging from 0.55 % around 630 nm to 0.3 % at 690 nm. An average reflectivity

function  $R_{avg}(\lambda)$  peaking at  $R_{avg}(620 \text{ nm}) = 0.9987 \pm 1.5 \times 10^{-4}$  was calculated from all individual measurements during NO3Comp and applied for the retrieval of the NO<sub>3</sub> mixing ratios.

395 A singular value decomposition algorithm was used for the retrieval of the absorber mixing ratios from a linear combination of the reference spectra (convoluted for 0.6 nm spectral resolution) and a second order polynomial represented broadband spectral structures,  $\alpha_{bb}(\lambda) = n_0 + n_1\lambda + n_2\lambda^2$ , resulting mainly from aerosol extinction.

$$\alpha(\lambda) = \alpha_{bb}(\lambda) + \sum_i \sigma_i(\lambda) \cdot \int_0^{L_{eff}} n_i(x) dx = \frac{1}{L_{eff}} \left[ \frac{I_0(\lambda)}{I(\lambda)} - 1 \right] (1 - R(\lambda)) \quad (4)$$

400 The fitting algorithm did not include O<sub>3</sub> because its absorption spectrum in the region of interest (655–670 nm) is weak and free of spectral fine structures, hence the broadband O<sub>3</sub> absorption was accounted for by the polynomial. To properly describe the complex absorption spectrum of water vapor, a concentration-corrected absorption cross section,  $\sigma'_{\text{H}_2\text{O}}(\lambda)$ , was calculated for each water concentration that occurred in experiments as described by Varma et al. (2009).

405 The overall accuracy of UCC-IBBCEAS was estimated to be  $\pm 16\%$ . This estimate took into account the standard deviation of the reflectivity measurements, the uncertainty of the NO<sub>3</sub> cross section and the effective cavity length, fluctuations of  $I_0$  and a 10 % uncertainty of various analysis approaches (choice of fit range and weighting). The measurement precision was given as percentage error of the NO<sub>3</sub> mixing ratio determined from the 1 $\sigma$ -standard deviation of the fit residuals. The

410 1 $\sigma$ -detection limit is estimated to be 1 pptv for a 5 s averaging time.

### 2.1.6 Cavity enhanced DOAS, UHD-CEDOAS

The University of Heidelberg (Germany) CEAS-based DOAS instrument used a short open-path setup and was installed inside the SAPHIR chamber mounted on a steel frame 60 cm above the floor in front of the fan. Except for the cavity mirrors all parts of the instrument were enclosed with Teflon  
415 foil to avoid surface reactions or out-gassing close to the optical absorption path. The optical setup and the specifics of the data evaluation of CEDOAS measurements is described in the publications by Meinen et al. (2010) and Platt et al. (2009), respectively.

The cavity consisted of two highly reflective mirrors (25.4 mm diameter and 1 m radius of curvature) with a nominal peak reflectivity of 99.9985 % at 655 nm. The separation of the mirrors was  
420 0.62 m, and the effective optical path length was reduced to  $0.5 \pm 0.01$  m by a purge flow of 5 slm of synthetic air. An LED (peak wavelength 665 nm, FWHM 23 nm), housed in a temperature stabilised box ( $300 \pm 2$  K), was mounted to one of the mirrors and the light was guided into the cavity by a 40 mm plano convex lens and a 610 nm long-pass filter (Schott RG610). Light leaking through the exit mirror was focussed into a 400  $\mu\text{m}$  quartz fibre (NA = 0.22, 5 m length). The fibre was at-  
425 tached alternatively to a photomultiplier tube (PMT) or to a temperature stabilised mini-spectrograph ( $273 \pm 0.1$  K, spectral resolution 1.06 nm), both placed outside the chamber, for time resolved (CRD) or wavelength dispersed measurements (CEAS), respectively. Typical signal averaging times were

300 s.

Data evaluation was based on the classical DOAS approach (Platt and Stutz, 2008). In DOAS ap-  
430 plications the length of the absorption light path is well known and constant. In combination with an  
optical cavity (CEDOAS), however, the effective path length that photons travel in the optical cavity,  
 $X_{eff}$ , can be highly variable because  $X_{eff}$  depends not only on the wavelength dependent reflec-  
tivity finesse of the cavity,  $F = \pi\sqrt{R(\lambda)}/(1 - R(\lambda))$  (Triki et al., 2008), but also on broad-band  
losses by Mie and Rayleigh scattering, as well as on the mixing ratios of all absorbing constituents  
435 contributing to the total extinction in the cavity (cf. Platt et al., 2009).

The effective mirror reflectivity,  $R_{eff}(\lambda)$ , was determined daily from measurements of the cavity  
ring-down decay in pure synthetic air using the LED in pulsed mode. The multi-exponential time  
dependent decay of the cavity intensity was modelled after Meinen et al. (2010, Eq. (4b)) using the  
cavity transmission spectrum measured in CEAS mode (which reflects the LED emission spectrum  
440 folded by the unknown 'true' mirror reflectivity function) and the wavelength dependent mirror  
reflectivity,  $R_M(\lambda)$ , provided by the mirror manufacturer. A single scaling factor  $a$  and an offset  
 $b$  were fitted to the modelled decay function in order to reproduce the measured time decay. The  
effective ('true') mirror reflectivity  $R_{eff}$  was obtained by  $R_{eff}(\lambda) = a \times R_M(\lambda) + b$  assuming the  
shape of the mirror reflectivity  $R_M(\lambda)$  to be invariant. The effective path length in the cavity at the  
445  $\text{NO}_3$  absorption maximum in zero air, required for the DOAS evaluation process, was calculated  
according to ( $L$  = mirror separation)

$$X_0(662nm) = \frac{L}{1 - R_{eff}(662nm)} \quad (5)$$

Typical values during NO3Comp were  $8400 \text{ m} \pm 100 \text{ m}$  (09...18 June) and  $8700 \text{ m} \pm 300 \text{ m}$  (on 20  
and 21 June).

450 The CEDOAS  $\text{NO}_3$  data retrieval required several steps. (1) Zero air spectra  $I_0(\lambda)$  were recorded  
in the morning of each day of the campaign in the clean flushed SAPHIR chamber containing only  
dry synthetic air (dew point  $< 220 \text{ K}$ ). (2) During the running experiment, the time series of mea-  
surement spectra  $I_m(\lambda, t)$  with absorbers (and aerosol extinction, in case of their presence) were  
recorded and the resulting optical density  $D_{CE}(t)$

$$455 D_{CE}(t) = \ln\left(\frac{I_0(\lambda)}{I_m(\lambda, t)}\right) \quad (6)$$

was determined. Literature reference spectra of the present trace gases deconvolved to the spectral  
resolution of the instrument and a second order polynomial accounting for all broadband absorption  
effects were fitted to the differential structures of the spectra according to the classical 'DOAS pro-  
cedure' (Platt and Stutz, 2008). The trace gas concentrations  $C_0$  were obtained from the retrieved  
460 column densities using the actual path length  $X_0(662nm)$  of the respective day. In the case of small  
trace gas absorption and aerosol-free conditions the mixing ratios are properly accounted for. (3) If,  
however, light losses due to broadband and/or narrowband extinction processes were larger, i.e.,  
during the aerosol experiments, the effective path length in the cavity was reduced and consequently

the mixing ratios  $C_0$  had to be corrected according to the procedure described by Platt et al. (2009,  
465 Eq. (41))

$$C_{true} = C_0 \frac{e^{D_{CE}} - 1}{D_{CE}} \quad (7)$$

As this correction relies on the absolute optical density, the long-term stability of the light source be-  
comes of importance. A scatter plot of the intensities of all zero air spectra  $I_0(\lambda)$  acquired during the  
intercomparison, normalised to 1 ms integration time, showed a linear decrease with time (correla-  
470 tion coefficient  $r = -0.991$ ). The corresponding zero intensity  $I_0(\lambda, t)$  for each  $\text{NO}_3$  measurement  
at time  $t$  during the campaign (to be used in Eq. 6) was calculated using the linear regression line  
through this data.

The typical precision of the CEDOAS technique varied between 3 and 6 pptv ( $1\sigma$ ) for a data  
acquisition time of 5 min with the larger value for experiments with high water vapor concentrations  
475 or in the presence of high aerosol load. The total measurement accuracy was 12 % and takes into  
account a 3 % error of the light path length  $X_0$  calculation, 10 % uncertainty of the cross section,  
5 % error of the effective cavity length, and the correction of the reduced path length of 3 %.

### 2.1.7 Differential Optical Absorption Spectroscopy, FZJ-DOAS

Forschungszentrum Jülich used broadband Differential Optical Absorption Spectroscopy (DOAS)  
480 for in situ  $\text{NO}_3$  measurements in SAPHIR. DOAS allowed for the separation of overlapping narrow-  
band spectral structures of different atmospheric constituents with high selectivity (fingerprint de-  
tection). DOAS is 'immune' against continuous (broad-band) extinction processes caused by mirror  
coatings, Rayleigh and aerosol scattering (Platt and Stutz (2008)). The setup of the FZJ-DOAS  
instrument at SAPHIR has been described in Bossmeyer et al. (2006) and Brauers et al. (2007).

485 A Xenon short arc lamp (OSRAM, XBO75W/2, arc size  $0.3 \times 0.5 \text{ mm}^2$ ) housed outside the cham-  
ber served as a light source. The light was collected in a fiber (400  $\mu\text{m}$ , 2 m length) and transferred  
to the chamber via a telescope. The light entered and left the chamber through a quartz window.  
Inside the chamber the light traveled 48 times within a modified version of a White type multiple re-  
flection system of 20 m base length (Doussin et al., 1999) equipped with enhanced aluminum coated  
490 mirrors (average reflectivity  $\approx 0.94$  between 600 and 700 nm). The optical components of the White  
cell were setup at the North and South sides of the chamber. After leaving the White cell, the light  
passed through a long-pass color filter (Schott, OG530) to block excess light from entering the spec-  
trograph. The light was guided via an optical fibre assembly into a temperature stabilised ( $\pm 0.25 \text{ K}$ )  
Czerny-Turner type spectrograph (spectral resolution 0.4 nm) equipped with a linear photo diode ar-  
495 ray (1024 pixels, 25  $\mu\text{m}$  width) detecting a spectral range from 601 to 690 nm. The spectra recording,  
handling and fitting was controlled by the DOASIS software package (Kraus, 2006).

The  $1\sigma$  precision of the measurements was approximately 10 pptv for 1 min data acquisition time.  
The accuracy depended mainly on the uncertainty of the  $\text{NO}_3$  cross section (5 %,  $1\sigma$ ). During the

campaign an additional systematic variability by  $\pm 20$  pptv was observed in the retrieved  $\text{NO}_3$  mixing ratios which was taken additionally into the accuracy. The fluctuations were most likely caused by intermittent shifts of the arc emission point on the surface of the electrodes of the Xe lamps used during NO3Comp.

## 2.2 Atmosphere Simulation Chamber SAPHIR

The SAPHIR chamber has been primarily designed for the controlled investigation of atmospheric chemical reaction systems under conditions similar to those in the ambient atmosphere, by using typical mixing ratios of trace gas constituents. SAPHIR is also optimally suited for the comparison of sensitive instruments for atmospheric trace gas and radical measurements. Unknown interferences do not affect the measurements as the composition of the air is known and the well mixed air in the chamber allows for comparable measurements of all participating instruments (e.g. Schlosser et al., 2007, 2009; Fuchs et al., 2010b,a; Rohrer et al., 2005; Bossmeyer et al., 2006; Brauers et al., 2007; Wegener et al., 2007).

The SAPHIR chamber consists of a double-walled Teflon FEP (DuPont) bag of cylindrical shape (length 18 m, diameter 5 m, effective volume  $270 \text{ m}^3$ , surface/volume  $\approx 1 \text{ m}^{-1}$ ) that is held by a steel frame. The space between the inner and the outer tube (15 cm) is permanently flushed with ultra clean nitrogen (purity  $>99.9999 \%$ ) to prevent diffusion of gases from outside. The inner volume is always held 40 Pa over ambient pressure in order to avoid contamination with outside air and to keep the FEP film under tension. Losses by gas extraction by the instruments and small leaks are compensated for by a replenishment flow rate of 10 to  $15 \text{ m}^3/\text{h}$  which dilutes all constituents in the chamber at a rate of 3.5 to  $5.5 \%$   $\text{h}^{-1}$ . The actual dilution is monitored by a flow controller and additionally by a gas-chromatographically measurement of an inert tracer (ethane) added to the chamber air. The chamber is housed within completely retractable metal blinds that keep the chamber in darkness as required for the detection of  $\text{NO}_3$  radicals. The blinds can be opened if daylight exposure is needed (i.e., in  $\text{NO}_3$  photolysis experiments). In order to minimise potential photolysis of  $\text{NO}_3$  during daylight measurements all flanges and other light leaks were carefully covered by black foil resulting in a reduction of the  $\text{NO}_3$  photolysis frequency in the chamber to  $\ll 10^{-4}$  of the outside value.

The SAPHIR chamber is equipped with a comprehensive set of sensitive instruments comprising measurements of temperature, pressure, and humidity. NO and  $\text{NO}_2$  are measured by chemiluminescence,  $\text{O}_3$  is measured by UV absorption (Ansyco) and by chemiluminescence (modified ECO Physics CLD AL 700). Volatile organic compounds (VOC) are measured by Gas Chromatography using a flame ionisation detector (Chrompack) (Wegener et al., 2007) and by proton transfer reaction mass spectrometry (PTR-MS, IONICON, Austria) (Lindinger et al., 1998). An ultrasonic anemometer (USA) measures the gas temperature inside the chamber with an accuracy of  $\pm 0.2 \text{ K}$ .

Aerosol number densities and size distributions were measured with a Water Condensation Par-

535 ticle Counter (TSI WCPC model 3785) and a Scanning Mobility Particle Sizer (TSI SMPS 3936,  
consisting of a Differential Mobility Analyser (DMA 3081) and a WCPC 3785). The time resolu-  
tion was 20 s for the CPC measurements and 7 min for the SMPS. A time-of-flight aerosol mass  
spectrometer (Aerodyne TOF-AMS) was operated to measure the aerosol chemical composition  
(Canagaratna et al., 2007). The AMS was connected to the SAPHIR chamber via a stainless steel  
540 tube designed to minimise losses in the sampling line (Fry et al., 2009).

Before each experiment, the chamber was purged with dry synthetic air overnight (from liquid N<sub>2</sub>  
and O<sub>2</sub>, purity >99.9999 %, flow rate up to 500 m<sup>3</sup>/h) to parts per trillion (pptv) levels of nitrogen  
oxides, ozone, and hydrocarbons. If required, high purity water (Milli-Q Gradient A10, Millipore  
Corp.) was evaporated in a steam generator and added to the purge flow at the end of the flushing of  
545 the chamber until the required humidity was reached. The trace gases (O<sub>3</sub>, NO<sub>2</sub>, and hydrocarbons)  
were added to the replenishment flow. The inlet port was located at the northern end of SAPHIR  
at the main inlet which is also used to flush the chamber (Fig. 1). Ozone was produced by silent  
discharge in pure oxygen. Ammonium sulfate, (NH<sub>4</sub>)<sub>2</sub>SO<sub>4</sub>, aerosol was added directly by spraying  
an aqueous solution into the chamber using a nebuliser. For some experiments 500 ppmv of CO was  
550 added to the chamber before the reaction started in order to scavenge any OH radicals formed.

The homogeneity of the trace gas distribution in the chamber was established by a powerful fan  
which was mounted near the southern end of the chamber 1 m above the chamber floor. It was op-  
erated during all experiments. Measurements with the fan switched off showed noticeable mixing  
ratio differences between instruments which disappeared when the fan was running. Test measure-  
555 ments demonstrated that the inlet lines inside the chamber (lengths varied between 12 and 40 cm)  
sampled air from the well mixed volume so that potential surface gradients were negligible when the  
fan was running. The absence of concentration gradients under well mixed conditions was already  
demonstrated during the intercomparison of OH/HO<sub>2</sub> detection instruments (Schlosser et al., 2009)  
where different OH instruments sampled air from 2 cm to 170 cm above the chamber floor.

560 Figure 1 shows the positions of the NO<sub>3</sub> instruments at SAPHIR. FZJ-DOAS, UCC-IBBCEAS,  
and UHD-CEDOAS detected NO<sub>3</sub> in situ inside the chamber. While the UHD-CEDOAS open  
path instrument was setup 60 cm above ground, the absorption light paths of FZJ-DOAS and UCC-  
IBBCEAS extended along the central axis, about 1.7 m above the floor of SAPHIR. All other instru-  
ments were located beneath the chamber and sampled the chamber air through individual ports in  
565 the floor.

### 2.3 Intercomparison experiments

Chamber measurements were carried out in simple reaction mixtures to assess accuracy, precision,  
detection limits, and time response of the participating instruments. The experiments were per-  
formed in order of increasing chemical complexity. They were also designed to study the influence  
570 of species that potentially affect the measurement principles or retrieval approaches of the various

instruments. Starting with water vapor and NO<sub>2</sub> (09 to 13 June), followed by organic molecules and their oxidation products (14 to 21 June), the influence of inorganic aerosol (15 and 18 June), and secondary organic aerosol (SOA) formed during in situ experiments (16, 20, 21 June) was investigated (see Table 1). To test the instruments under realistic conditions, ambient air was pumped into the chamber on 11 June. All simulation studies were performed under ambient pressure and temperature so that the performance of the instruments was investigated under realistic, near-atmosphere conditions.

Experiments usually started by adding NO<sub>2</sub> and O<sub>3</sub> into the either dry or humidified synthetic air of the chamber. Maximum NO<sub>3</sub> mixing ratios established typically after an hour. In many experiments the chemical system was 'refuelled' after some time by a second addition of NO<sub>2</sub>, O<sub>3</sub> or both. Fast modulations of the NO<sub>3</sub> mixing ratio were initiated by the injection of reactive hydrocarbons (16, 18, 20, 21 June) or by photolysis with ambient sunlight after opening the shutters of the SAPHIR chamber (12, 13 June and at the end of most experiments in the afternoon).

### 3 Observations and results

#### 3.1 Precision of the instruments

The instrumental precision was a key parameter required for a statistically sound regression analysis. The precision of the instruments was investigated under conditions of vanishingly small NO<sub>3</sub> mixing ratios. All measurements in the clean chamber after flushing with synthetic air over night ('zero air' data) were included but also NO<sub>3</sub> data during the preparation phase of the experiments were selected, i.e., times were chosen when the chamber air already contained hydrocarbons, ozone or NO<sub>2</sub> (aerosol excluded), but in any case, before the formation of NO<sub>3</sub> was initiated.

In Fig. 2 the frequency distributions of zero NO<sub>3</sub> measurements are shown. The optimal bin size to be used for the histograms depends on the sample size and the spread of the data range and was selected after Freedman and Diaconis (1981). A Gaussian distribution of the same area as the measured data was fitted to the histograms to visualise the mean of the zero measurements and their standard deviation, which is a measure of the actual instrumental precision. The histogram of the MPI-CRDS instrument is not included because the number of available zero air data ( $n = 7$ ) was too small for a meaningful statistics. The calculated values of Skewness and Kurtosis for the histograms of UCC-IBBCEAS and UAF-CRDS (1.36/3.43 and 0.92/3.46, respectively) show significant differences from zero which indicate that these two data sets are most likely not normal distributed.

NOAA-CRDS (time resolution  $\Delta t = 1$  s), UAF-CRDS ( $\Delta t = 1$  s), ULEIC-BBCRDS ( $\Delta t = 1$  min), and UCC-IBBCEAS ( $\Delta t = 5$  s) show excellent precision in the range of 0.5 to 2 pptv, and the calculated mean NO<sub>3</sub> mixing ratios deviate no more than  $\pm 0.2$  pptv from zero. The precision of UHD-CEDOAS ( $\Delta t = 5$  min) and FZJ-DOAS ( $\Delta t = 1$  min) is in the range 5 to 10 pptv, and the mean of the frequency distributions is biased to marginally higher values ( $\approx 2$  to 4 pptv, respectively). The

precision of the MPI-CRDS instrument ( $\Delta t = 10$  s), as estimated from visual comparison of measurements at  $\text{NO}_3$  mixing ratios  $< 35$  pptv on 16 June (Fig. 4), is comparable to the other CRDS instruments.

In part (a) of Table 2 the mean  $\text{NO}_3$  mixing ratio is compared with the corresponding confidence interval  $2\sigma/\sqrt{n}$ . Given the high precision of the measurements and the large number of data points  $n$ , the observed deviation from zero is extremely small but statistically significant for all instruments except ULEIC-BBCRDS whose observed deviation at zero is within the uncertainty interval. The lower part (b) of the table compares the mean of the errors of zero- $\text{NO}_3$  measurements ( $\langle\sigma\rangle$ ) with the precision calculated from the frequency distribution of zero data ( $1\sigma$ -width of the Gaussian distribution in Fig. 2). Within the calculated uncertainty no significant difference can be found, meaning that the a priori estimation of the measurement errors by the operators of each instrument correctly describe the statistical variation of the instruments.

### 3.2 Time series of $\text{NO}_3$ measurements

Time series of  $\text{NO}_3$  mixing ratios for each day are presented in the upper panels of Figs. 3 and 4. The  $\text{NO}_3$  data are plotted with the original time resolution that each instrument's data was reported, without any further averaging or filtering (NOAA-CRDS 1 s, UAF-CRDS 1 s, UCC-IBBCEAS 5 s, MPI-CRDS 10 s, FZJ-DOAS 60 s, ULEIC-BBCRDS 61 s, and UHD-CEDOAS 300 s). Error bars are omitted for clarity. The lower panels for each day show mixing ratios of key constituents such as  $\text{NO}_2$ ,  $\text{O}_3$ , and hydrocarbons, as well as other relevant parameters like the water vapour partial pressure, and the total aerosol surface concentration. Grey vertical dashed lines in the  $\text{NO}_3$  panels indicate times when the roof of the SAPHIR chamber was opened (and closed again) to detect the fast decrease of  $\text{NO}_3$  due to photolysis (and its subsequent reformation).

$\text{NO}_3$  mixing ratios throughout the campaign were below 250 pptv with three exceptions on the 'photolysis days' (12 and 13 June, 350 pptv and 700 pptv) and on the 'SOA day' (20 June, 400 pptv). Exceptionally low  $\text{NO}_3$  mixing ratios occurred on 16 June ( $\leq 40$  pptv) and especially on 18 June when  $\text{NO}_3$  mixing ratios remained between 2 pptv after the first isoprene injection and 12 pptv after a second addition (see Fig. 4). Prior to the discussion of the individual  $\text{NO}_3$  time series of each experiment of the campaign, some discernible features in the figures merit discussion.

1.  $\text{NO}_3$  mixing ratios measured by UCC-IBBCEAS on 10, 11, 13, 15, and 20 June significantly differed from the values of all other instruments (Fig. 3). A similar observation for the UCC instrument was described by Fuchs et al. (2010a) for the comparison of  $\text{NO}_2$  measurements performed during NO3Comp. The systematic difference of the  $\text{NO}_3$  mixing ratios can be explained by the fact that on those days no measurements of zero air background spectra ( $I_0(\lambda)$ , Eq. (3)) could be taken in the morning before the experiments for following reasons. On 10, 15, and 20 June,  $\text{NO}_3$  was already produced in the chamber before the UCC-IBBCEAS instrument was operational, on 11 June ambient air was pumped into the chamber, and on 13 June the previous

experiment was continued over night without flushing in the morning. Zero air spectra from the day after or before were used for the retrieval of the  $\text{NO}_3$  mixing ratios in these cases. Notably, differences in the  $\text{NO}_3$  mixing ratio measured by UCC-IBBCEAS and other instruments are expected to be the largest on days when the background spectrum could not be measured. This indicates that the long-term drift of the lamp was a limiting factor for the UCC-IBBCEAS instrument during some experiments of NO3Comp.

2. Mixing ratios taken with the ULEIC-BBCRDS instrument on 10 June were exceptionally low (orange diamonds in Fig. 3). At the end of the experiment it was noticed that the sampling line had collapsed. Therefore it had to be assumed that during the experiment the flow rate was potentially already much smaller than expected resulting in enhanced losses of  $\text{NO}_3$  in the instrument.
3. On 11 June the ULEIC-BBCRDS data exhibited the strongest fluctuations during NO3Comp. The amount of ambient air that was found to be leaking into the BBCRDS cavity (see Sect. 2.1.4) was highly variable, ranging between 0 and 30 %. Quantitative correction of the dilution effect was difficult to achieve under these conditions resulting in less precise measurements on that day.
4. Also the performance of the UHD-CEDOAS instrument was degraded on 11 June in the morning. The chamber was flushed with open roof leading to an overheating of the LED light source by solar radiation. The induced drift of the LED output made the spectral retrieval unreliable as demonstrated by the large positive offset of the  $\text{NO}_3$  data before 09:45 UTC (Fig. 3).
5. On 9 June (14:38 UTC) and on 12 June (12:46 UTC) the fan inside the chamber was switched off some time before the roof was opened. In stagnant air, the mixing time in the dark chamber is in the order of an hour. This is considerably longer than the  $\text{NO}_3$  lifetime of 30 min (Fry et al., 2009) in the dry chamber, making wall reactions of  $\text{NO}_3$  a significant loss process and enabling measurable concentration gradients to build up. Consequently, these episodes of inhomogeneous sampling conditions were excluded from further data analysis.

In order to get a representative picture of the instrument performance throughout the campaign, the data on these occasions where specific instrument issues have been identified are still included in calculating the full-campaign correlations (except 5.). The following paragraphs describe the time series of the  $\text{NO}_3$  mixing ratios recorded during NO3Comp. An brief summary of the typical mixing ratios of key constituents observed during the experiments is given in Table 1.

*9 June, 10 June:* During the first part of the campaign (09...14 June) the majority of measurements were carried out in simple reaction mixtures. On 09 and 10 June a potential cross interference of  $\text{NO}_2$  and water vapour was investigated, respectively. With the exception of the scenarios discussed above the  $\text{NO}_3$  mixing ratios of all instruments agree well and mostly overlap within their errors. On 10 June the data of the UHD-CEDOAS instrument tend to lower values at higher water vapour mixing ratios possibly because the light path reduction due to water vapor was not taken into

account correctly.

680 *11 June:* An experiment with ambient aerosol was performed on 11 June. The chamber was flushed with ambient air while the roof was open in order to avoid NO<sub>3</sub> formation during the flushing period. A filter (cut-off size unknown) removed coarse-mode particles. The resulting aerosol surface concentration was very low and did not vary much ( $(1.3...0.5) \times 10^7 \text{ nm}^2 \text{ cm}^{-3}$ ) during the experiment (Fig. 3). The aerosol mass spectrometer could not measure due to the low particle concentration, therefore chemical properties of the aerosol are unknown. Peak mixing ratios of NO<sub>2</sub>,  
685 O<sub>3</sub>, and water after closing the roof at 08:01 UTC were 23 ppbv, 25 ppbv, and 1.7 %, respectively. At 09:04 UTC formation of NO<sub>3</sub> was stimulated by addition of 70 ppbv O<sub>3</sub> into the dark chamber. Technical problems affected UHD-CEDOAS, ULEIC-BBCRDS, and UCC-IBBCEAS (see above), but NOAA-CRDS, FZJ-DOAS, and UAF-CRDS data were very similar throughout the day.

690 *12 and 13 June:* On these 'photolysis days' the NO<sub>3</sub> production rate was high and the chemical losses were low, leading to the largest NO<sub>3</sub> mixing ratios of the campaign (700 pptv on 13 June). NO<sub>3</sub> was frequently photolysed on both days by opening and closing the roof system of the SAPHIR chamber. The photolytic lifetime of NO<sub>3</sub> was approximately 5 s when the roof was open; however the observed NO<sub>3</sub> lifetime was approximately one minute because the fast thermal dissociation of N<sub>2</sub>O<sub>5</sub> (present at  $\approx 2$  ppbv (Fuchs et al., 2012)) acted to partially buffer the NO<sub>3</sub> lost to photolysis. Figure 3 clearly demonstrates the very good time resolution of the 'faster' instruments NOAA-CRDS, UAF-CRDS, UCC-IBBCEAS, and MPI-CRDS, which were able to detect the quick changes  
695 of NO<sub>3</sub> very accurately.

700 *14 June:* In this experiment the oxidation of butanal by NO<sub>3</sub> was studied. The measurements revealed very good agreement between the instruments. However, the sensitivity of the UHD-CEDOAS instrument seemed to have changed after 10:00 UTC.

705 *15 June:* During this experiment ammonium sulfate aerosol was generated and added twice during 10:45–11:25 and 12:30–14:55 UTC (black dotted lines in Fig. 4) by spraying an aqueous solution into the clean humidified (60 % RH) chamber using a nebuliser. Peak aerosol surface concentrations of  $3 \times 10^8 \text{ nm}^2 \text{ cm}^{-3}$  and  $5.8 \times 10^8 \text{ nm}^2 \text{ cm}^{-3}$ , corresponding to  $5 \mu\text{gm}^{-3}$  and  $12 \mu\text{gm}^{-3}$ , respectively, were reached at the end of the injection periods. During the humidification of the aerosol-free chamber air (starting at 09:00 UTC) the mixing ratio of NO<sub>3</sub> dropped to zero. The addition of O<sub>3</sub> and NO<sub>2</sub> at 09:56 UTC brought the NO<sub>3</sub> mixing ratio back up to about 110 pptv (Fig. 4). The first aerosol generation began at the maximum of the NO<sub>3</sub> mixing ratio which then decreased to about 50 pptv due to the enhanced dilution of the chamber air by the high air flow through the aerosol generator. At the start of the aerosol addition the readings of UHD-CEDOAS, ULEIC-BBCRDS, and UAF-CRDS corresponded well (115 pptv at 10:45 UTC) while UCC-IBBCEAS and FZJ-DOAS measured 135 pptv and NOAA-CRDS was lowest at 100 pptv. After the first aerosol addition was finished (11:25 UTC), the NO<sub>3</sub> mixing ratios reported by ULEIC-BBCRDS, UHD-CEDOAS, and particularly by UAF-CRDS significantly had dropped below the NOAA-CRDS readings. During

715 the subsequent second particle injection, the aerosol surface concentration nearly doubled but no  
further significant change of the relation between NOAA-CRDS and the other instruments was ob-  
served, except for the ULEIC-BBCRDS instrument.  $\text{NO}_3$  data measured after 13:45 UTC until the  
end of the experiment agreed well with the NOAA reference instrument but were lower by about  
16 pptv prior to this. Most likely the pronounced underestimation of the  $\text{NO}_3$  mixing ratio before  
720 13:45 UTC was caused by an intermittent problem with a leak as a comparison of the ULEIC water  
vapour data with a dew point hygrometer inside SAPHIR suggested. The FZJ-DOAS instrument  
showed excessive fluctuations caused by the unsteady arc of the Xe high pressure lamp making the  
 $\text{NO}_3$  measurements unreliable on 15 June.

*16 and 17 June:* During this two-day experiment the limonene- $\text{NO}_3$  reaction and the for-  
725 mation of products, both in the gas and in the particulate phase were studied (Fry et al., 2011).  
Limonene (10 ppbv) was already injected before  $\text{NO}_3$  was generated, so that the  $\text{NO}_3$  mixing ra-  
tio remained suppressed below the detection limit of all instruments. After limonene was fully  
consumed, the ongoing reaction between  $\text{NO}_2$  and  $\text{O}_3$  caused  $\text{NO}_3$  mixing ratios to rise to about  
35 pptv. About  $10 \mu\text{g}/\text{m}^3$  of aerosol was formed resulting in an aerosol surface concentration of  
730  $3 \times 10^8 \text{ nm}^2 \text{ cm}^{-3}$ . Data from all instruments compare well under these conditions, except for FZJ-  
DOAS and UCC-IBBCEAS which showed a trend to slightly higher  $\text{NO}_3$  mixing ratios (difference  
remained  $< 5$  pptv). The FZJ-DOAS instrument was close to the detection limit ( $S/N \approx 1$  to 3) on  
that day. The second limonene injection at 15:00 UTC on 16 June occurred almost simultaneously  
with the addition of  $\text{NO}_2$  and  $\text{O}_3$ . During the second oxidation step further aerosol was formed peak-  
735 ing at  $24 \mu\text{g}/\text{m}^3$  ( $4 \times 10^8 \text{ nm}^2 \text{ cm}^{-3}$ ). As expected,  $\text{NO}_3$  started to rise again quickly after limonene  
was consumed. The observed unexpected decrease of the  $\text{NO}_3$  mixing ratio reaching a minimum at  
18:00 UTC (Fig. 4) was due to complex coupling of the chemistry in the gas phase with that of the  
organic particle phase and has not been fully understood yet (Fry et al., 2011). ULEIC, MPI, and  
UHD finished measurements at 13:30, 15:50, and 16:40 UTC, respectively, before the  $\text{NO}_3$  mix-  
740 ing ratios again began to rise up until midnight. During the last six hours of the 16 June data the  
differences between the readings of the remaining instruments increased.

NOAA-CRDS, UCC-IBBCEAS and FZJ-DOAS continued their measurements until 17 June,  
19:00 UTC. No aerosol measurements were available for that day. UAF-CRDS commenced mea-  
surements again at 08:00 UTC after the replacement of an aerosol filter. With a new filter in the inlet  
745 the instrument detected slightly larger  $\text{NO}_3$  mixing ratios than NOAA-CRDS while the opposite  
was the case on 16 June, indicating a potential loss of  $\text{NO}_3$  by aerosol particles deposited on the  
UAF-CRDS instrument's filter surface.

*18 June:* The oxidation of isoprene by  $\text{NO}_3$  in the presence of ammonium sulfate seed aerosol  
was studied on 18 June (Rollins et al., 2009). The first isoprene injection (10 ppbv at 07:40 UTC)  
750 was made before any  $\text{NO}_3$  was generated (the  $\text{NO}_3$  production started after ozone injection at  
08:48 UTC) and the second isoprene injection (10 ppbv at 16:11 UTC) occurred two hours after the

system was refuelled by NO<sub>2</sub> and O<sub>3</sub> addition. In the first part of the experiment the NO<sub>3</sub> mixing ratio reached peak values of only 2 pptv and at the end of the experiment at midnight NO<sub>3</sub> was less than 12 pptv, still close to the detection limit of FZJ-DOAS and UHD-CEDOAS. The aerosol surface concentration in the morning reached  $1.3 \times 10^8 \text{ nm}^2 \text{ cm}^{-3}$ , about 20 % of the maximum value on 15 June, and gradually decreased to  $0.2 \times 10^8 \text{ nm}^2 \text{ cm}^{-3}$ . The fast increase of NO<sub>3</sub> after mid-afternoon refuelling additions of NO<sub>2</sub> and O<sub>3</sub> was very well captured by all instruments. NO<sub>3</sub> mixing ratios detected by UCC-IBBCEAS appear to be 5–10 % higher before isoprene was injected.

*20 and 21 June:* On the last two days of the campaign the oxidation of  $\beta$ -pinene in dry air and at 60 % RH, respectively, was investigated. After the injection of  $\beta$ -pinene the NO<sub>3</sub> mixing ratio dropped to 20 pptv and 5 pptv, respectively, and remained suppressed until the hydrocarbon had reacted completely. Prompt SOA formation was observed reaching a maximum concentration of  $40 \mu\text{g m}^{-3}$ , corresponding to an aerosol surface concentration of  $5.6 \times 10^8 \text{ nm}^2 \text{ cm}^{-3}$ , about 45 min and 90 min, respectively, after injection of the hydrocarbon (Fry et al., 2009). After the consumption of  $\beta$ -pinene, the NO<sub>3</sub> mixing ratio increased again to a maximum of 400 pptv and 80 pptv, respectively. During this period the high precision of the instruments allowed the investigators to visualise an increasing difference in the NO<sub>3</sub> mixing ratios as measured by the instruments over time. A detailed discussion will follow in Sections 3.3.3 and 4.4.2.

### 3.3 Correlation and regression analysis

#### 3.3.1 Correlation procedure

In order to assess the performance of the individual instruments, all NO<sub>3</sub> data sets were compared to one selected instrument. We chose the NOAA-CRDS NO<sub>3</sub> measurements as the reference for the correlation analysis for three reasons. (1) The NOAA-CRDS instrument was the technically most advanced one (see Sect. 2.1.1). Its properties were comprehensively studied and characterised in detail before and after the campaign (Dubé et al., 2006; Osthoff et al., 2006; Fuchs et al., 2008). (2) The NOAA instrument measured on all days of the campaign and produced the most complete data set. (3) The instrumental precision and consequently the detection sensitivity and time resolution are excellent, so that potential features in the correlation plots can be clearly identified. Especially the latter property favoured NOAA-CRDS over FZJ-DOAS which would normally had been our preferred choice, because the DOAS instrument has no inlet - one of the major uncertainties of the other instruments. In addition, DOAS is known to be 'immune' against broad-band light losses caused by Mie scattering of particles, Rayleigh scattering, or by other broad-band absorbers in the atmosphere (Platt and Stutz, 2008). Unfortunately, the FZJ-DOAS measurements turned out to be unusually noisy and showed sudden systematic variations during many days. The latter were most likely due to instabilities of the Xe arc lamps used during NO<sub>3</sub>Comp. If DOAS were chosen as reference excessive noise would have been added to all regressions. A comparison of the results

of a regression analysis with FZJ-DOAS or NOAA-CRDS as reference instrument showed that the major conclusions drawn from the correlations did not depend on the choice of the reference. We would like to emphasise that our selection shall not imply that the NOAA-CRDS data are inherently  
790 correct.

The correlation and regression analysis presented in the following sections are based on data sets averaged to a 3 min time grid which allows to compare fast and slower instruments within common time intervals. It was verified that the choice of the averaging interval does not significantly affect the results. In order to minimise potential errors by imperfect mixing in the chamber, all NO<sub>3</sub> mixing  
795 ratios measured within a time interval of 5 min after injection of reactive trace gases (NO<sub>2</sub>, O<sub>3</sub>, and hydrocarbons) were removed from the analysis.

In case of multiple NO<sub>3</sub> data points within one averaging interval, the mean value was calculated and assigned to the centre of the time interval. Data of 'slower' instruments were assigned to the centre of the interval where they appeared. Whenever the observed variability of the NO<sub>3</sub> mixing  
800 ratios within the averaging interval was comparable with the individual measurement errors, the standard deviation of the error bars was taken as 1σ error of the mean. If the data variability was larger, the standard deviation of the mixing ratios was taken as the error bar of the mean value (Schlosser et al., 2009; Fuchs et al., 2010a).

A weighted linear regression line was calculated using the procedure 'fitexy' by Press et al. (1992).  
805 This regression is invariant with respect to a permutation of independent and dependent variable and takes into account the errors of both coordinates. Thus, the statistical weight of each data point is calculated from the a priori precision of the data of both the respective instrument and NOAA-CRDS. In order to assess the statistical relevance of the linear regression parameters and their errors, the chi-square ( $\chi^2$ ) value of the linear fit to the measurements was calculated. A rule of thumb is  
810 that a 'typical' value of  $\chi^2$  for a 'good' fit is  $\chi^2 \approx (n - 2)$  ( $n$ ...number of data pairs correlated) (cf. Press et al., 1992, chapter 15). Furthermore a 'goodness-of-fit' parameter  $q$  was calculated from the chi-square distribution for  $(n - 2)$  degrees of freedom. It denotes the statistical probability that the deviation of the  $\chi^2$  value (obtained for some particular data set) from the 'expected'  $\chi^2 = n - 2$  value can be explained within the individual 1σ measurement errors of the data pairs correlated. If  
815  $q$  is a very small probability, then the inherent variance of the data set is larger than the 'confidence interval' defined by the individual error bars. Possible causes are either (1) the assumption of a linear model is wrong, (2) the errors are non-normal distributed, or (3) the measurement errors are really larger than stated. As an order of magnitude estimate the assumption of a linear dependency between the instruments within the range of their given measurement errors is believable if  $q \geq 0.1$ . For  
820  $q \geq 0.001$ , the fit may be acceptable if the errors are non-normal distributed or have been moderately underestimated. If  $q < 0.001$ , a linear relationship within the specified errors can be called into question. However,  $q$  is a very sensitive quantity for underestimated measurement errors. Often truly wrong models will be rejected with vastly smaller values of  $q$  ( $10^{-18}$ ). The opposite extreme,

$q \approx 1$ , is almost always caused by overestimation of the measurement errors by the experimenter  
825 (Press et al., 1992).

### 3.3.2 Correlations of combined data sets

It was already indicated in Sect. 3.2 that the performance of some  $\text{NO}_3$  instruments could be affected by the presence of aerosol. A similar observation has been described by Fuchs et al. (2012) for the intercomparison of  $\text{N}_2\text{O}_5$  measurements during NO3Comp. Therefore the scatter plots and  
830 the correlation and regression analysis of the  $\text{NO}_3$  data will be presented in separate figures for aerosol-free (Fig. 5) and aerosol-containing experiments (Fig. 6). Each panel in Figs. 5 and 6 shows the entire campaign data set for the nominated instruments plotted as scatter plot against the NOAA-CRDS reference instrument. The figures visualise the total variability of the instrumental performance relative to the NOAA instrument and the regression results allow for a comparison of the  
835 'average response' of the instruments during NO3Comp. The individual days of the campaign are distinguished by colour coded symbols and the error bars denote the  $1\sigma$  precision. The data range is limited to 420 pptv to avoid any bias by the high  $\text{NO}_3$  mixing ratios on 13 June.

On average all instruments performed very well over the course of the intercomparison. The  $\text{NO}_3$  mixing ratios of all instruments are exceptionally well linearly correlated with NOAA-CRDS. The  
840 coefficients of determination,  $r^2$ , are  $> 0.955$  in all cases (Table 3), i.e., more than 95 % of the variance observed in the instruments' responses is explained by the variance of the reference instrument. Due to the large number of data points,  $n$ , all correlations are highly significant. However the regression analysis resulted in  $\chi^2$  values which are significantly larger than the number of degrees of freedom ( $n - 2$ ) (last column in Table 3). Accordingly  $q$  was  $< 10^{-10}$  in all cases and is therefore  
845 not listed in Table 3. This finding shows that the variance in the  $\text{NO}_3$  data set of each instrument, considered over the entire course of the campaign, was significantly larger as it would be expected from the high precision of the measurements. Obviously the daily variability of the instrumental response was larger than the data variability during the single days. Consequently, the use of the data precision as weighting factor is not a suitable measure for the investigation of the 'average'  
850 (linear) relationship between the instruments during NO3Comp. While the individual measurement errors during a specific chamber experiment can be assumed to be normally distributed with a mean zero and constant variance, the statistical distribution of the day-to-day variability of the 'calibration factors' is not known. As a consequence, for the days where  $\chi^2/(n - 2) \gg 1$  (i.e., when  $q$  is not acceptable), the 'fitexy' routine is not well suited to calculate correct values and errors of intercept  
855  $a$  and slope  $b$  (Press et al., 1992). A more appropriate non-parametric line fitting technique is to be used which makes no assumptions on the distribution function of the data and their errors. We applied the 'least-normal-squares, LNS' technique (Troutman and Williams, 1987) which minimises the sum of squared perpendicular distances between the data points and the regression line. LSN is invertible and a unique relation (slope and intercept) is obtained regardless which variable is chosen

860 to be dependent. In order to determine the goodness of the procedure for fitting the straight line, i.e.,  
the errors  $\sigma_a$  and  $\sigma_b$ , a bootstrap technique was used. Bootstrapping is a non-parametric approach to  
determine statistical properties of data sets that does not require distributional assumptions such as  
normally distributed errors (Efron and Tibshirani, 1993). An application of this method for the deter-  
mination of measurement errors in high-resolution DOAS spectroscopy was described by Hausmann  
865 et al. (1999). The total bootstrap procedure comprises three steps: (1) A large number  $m$  (typically  
 $m \approx 1000$ ) of independent replicas from the data set under investigation (selected  $\text{NO}_3$  instrument  
vs reference instrument) is created by drawing with replacement a random sample of data pairs of  
the original data set. (2) The linear regression parameters intercept  $a'$  and slope  $b'$  for each replica  
are calculated. (3) The standard deviations of the  $m$  values of  $a'$  and  $b'$ ,  $\sigma_{a'}$  and  $\sigma_{b'}$ , finally represent  
870 the errors of the intercept  $a$  and the slope  $b$  of the LNS correlation line. The LNS line fit parameters  
(the 'best-fit' linear regression) are highlighted in Table 3 and shown as dark-red solid lines in Figs. 5  
and 6. Significant deviations of slope and intercept between fitexy (solid grey lines in the figures)  
and LNS mainly result for large chi-squared test values ( $\gtrsim 15$ ). The 'best-fit' linear regression line  
represents the average instrumental response for the entire intercomparison.

875 The LNS regression analysis reveals small intercepts close to the specified precision of the instru-  
ments. The slopes of the linear regression lines vary less than 15 % around unity for the whole-  
campaign correlations with the known exception for UCC-IBBCEAS (problem of recording zero  
air background spectra). Between the experiments with and without aerosol a tendency to under-  
estimate the  $\text{NO}_3$  mixing ratios in the presence of aerosol can be found for all instruments except  
880 FZJ-DOAS which correlates very well with NOAA-CRDS, again demonstrating its insensitivity to  
broad-band light extinction by aerosol. Overall we can state that the slopes of the regression lines  
are all within the combined  $1\sigma$ -accuracies of the nominated test instruments and NOAA-CRDS. This  
demonstrates that the instrumental accuracy was very well determined by the experimentalists.

### 3.3.3 Day-to-day correlations

885 Day to day variations of the detection sensitivity or different responsivity of the instruments towards  
interferences become more apparent in scatter plots that compare data separated into individual  
days' experiments. Figures 7 and 8 show the correlations of  $\text{NO}_3$  data of all instruments versus  
NOAA-CRDS for each experiment of the  $\text{NO}_3$ Comp campaign (cf. Table 1). Error bars are omitted  
for clarity. In order to assess the effect of aerosol on the quality of the measurements on 11, and  
890 15 to 21 June, only  $\text{NO}_3$  data are compared which were recorded in the presence of aerosol.

The routine 'fitexy' was used for the correlation and regression analysis in all cases and the results  
are summarised in Table 4. For every day the slopes of the linear regression lines fitted to the data  
were within the limits of the combined accuracies of the instrument pairs (as based on the a priori  
uncertainty estimates provided for each instrument by its operators). Only on four days (10, 11,  
895 13, and 20 June) did the slopes of UCC-IBBCEAS slightly exceed these limits for reasons already

stated.

*9, 10 and 11 June:* The experiments on 9 and 10 will be discussed in detail in Sections 4.2 and 4.3. On 11 June data correlated very well during the measurements in ambient air ( $r^2 > 0.963$ ). The UAF-CRDS data are very well linearly correlated with NOAA-CRDS ( $q = 0.85$ ). The apparent linear  
900 correlation of UHD-CEDOAS was erroneously caused by the very large errors of the instrument on 11 June (see Sect. 3.2 and grey symbols in Fig. 6).

*12 and 13 June:*  $\text{NO}_3$  was completely photolysed several times during the clean air/photolysis days (12, 13 June). The large dynamic range of  $\approx 700$  pptv allowed for tests of the linearity of the instruments. The measurements correlated extremely well,  $r^2$  varied between 0.975 and 0.999. The  
905 linear regression analysis revealed very good linearity over the full dynamic range of  $\text{NO}_3$  mixing ratios on 13 June and insignificant intercepts.

*14 June:* The correlation and regression results on 14 June are very similar to 13 June. The  $\text{NO}_3$  data of the butanal oxidation experiment are well correlated ( $r^2$  was between 0.908 and 0.993). Although FZJ-DOAS and ULEIC-BBCRDS data were significantly offset by +22 and -14 pptv, re-  
910 spectively, the slopes of the regression lines (which ranged from 0.89 to 1.09) were still within the combined errors of the instrument pairs. For unknown reasons, the UHD-CEDOAS measurements revealed a change in sensitivity at 10:00 UTC (see Fig. 3, open black squares).

*15 June:* Addition of inorganic aerosol (ammonium sulfate) to the chamber air generally caused a larger variability in the  $\text{NO}_3$  data. On 15 June the scatter plots of UAF-CRDS, UCC-IBBCEAS,  
915 and ULEIC-BBCRDS showed a common pattern (see, for example, blue and grey circles in Fig. 8). The first addition of aerosol began at the maximum of the  $\text{NO}_3$  mixing ratio (10:45 UTC) which then decreased to about 50 pptv when the first particle injection ended (11:25 UTC, cf. Fig. 4). During the injection period the  $\text{NO}_3$  values of all instruments correlated well with the NOAA-CRDS mixing ratios. The course of the  $\text{NO}_3$  data pairs can be described by 'trend lines' with a slope specific for each instrument. After the end of the aerosol injection, however, the pattern changed. The  
920 mixing ratios measured during the following 10 to 15 min decreased stronger than expected from the trend observed before. After this 'transition period' all following  $\text{NO}_3$  mixing ratios measured after 11:40 UTC and during the second aerosol injection (12:30-14:55 UTC) are grouped around different 'trend lines' with significantly smaller slopes than in the beginning. Obviously the increasing  
925 concentration of aerosol led to the recording of larger inlet losses of  $\text{NO}_3$  for some instruments. The UAF-CRDS instrument measured the lowest  $\text{NO}_3$  mixing ratios of all instruments on this day. The slope of the linear regression line (comprising the full data set of this day) was 0.86, while the slopes of ULEIC-BBCRDS, UHD-CEDOAS, and FZJ-DOAS showed no large deviation from unity. The FZJ-DOAS instrument was affected by excessive fluctuations of the light source leading  
930 to a moderate correlation ( $r^2 = 0.707$ ), an offset of +28 pptv, and a slope of 0.92 (Table 4).

*16 and 17 June:* The experiment on 16 June was the first to include the in situ production of aerosol inside the SAPHIR chamber, in this case secondary organic aerosol (SOA) formed by  $\text{NO}_3$

oxidation of limonene (Fry et al., 2011). This experiment resulted in similar observations as made in the inorganic aerosol study on 15 June. During the first oxidation step, at low aerosol concentrations, the data could be described by a line with a different slope than the NO<sub>3</sub> mixing ratios measured after the second injection of limonene (see UCC-IBBCEAS (blue circles) and UAF-CRDS (grey circles) in Fig. 8). The data are still highly correlated ( $r^2 = 0.959$  and  $0.965$ , respectively) and the slopes of the regression lines (1.17 and 0.91, respectively) are within the combined uncertainties of the instruments. FZJ-DOAS and UHD-CEDOAS correlate moderately ( $r^2 = 0.75$  and  $0.59$ , slopes = 1.02 and 1.02, respectively) due to the low signal-to-noise ratio (relatively small NO<sub>3</sub> mixing ratios were produced by this experiment), however the FZJ-DOAS data are well linearly correlated with unity slope. ULEIC-BBCRDS and MPI-CRDS stopped measurements already shortly before and after the second limonene injection. Owing to the lack of data from these instruments for high aerosol load the comparison is not particularly meaningful. NOAA-CRDS, UCC-IBBCEAS and FZJ-DOAS continued to record data overnight until 17 June, 19:00 UTC. UAF-CRDS commenced measurements again at 08:00 UTC with a new aerosol filter. For the instruments that were recording on 17 June, the NO<sub>3</sub> mixing ratios correlated very well with NOAA-CRDS, slopes were all  $\geq 1.1$  and intercepts were negligible ( $< 1.2$  pptv).

*18 June:* This experiment divides into two phases. As shown in Fig. 4, the NO<sub>3</sub> mixing ratio was smaller than 3 pptv in the morning and less than 12 pptv in the afternoon due reaction with isoprene. Only during a two hour period, after the addition of extra NO<sub>2</sub> and O<sub>3</sub> at 14:25 UTC, the NO<sub>3</sub> mixing ratio increased to 150 pptv. The comparison of the UAF-CRDS, UCC-IBBCEAS, and ULEIC-BBCRDS instruments with NOAA-CRDS showed coefficients of correlation close to unity during the interval of high NO<sub>3</sub>. A slope of 0.95 ( $r^2 = 0.998$ ), 1.06 ( $r^2 = 0.999$ ), and 1.02 ( $r^2 = 0.997$ ) were determined, respectively. The scatter plot of the time intervals of very low NO<sub>3</sub> mixing ratios (08:00-14:00 UTC and 16:30-23:50 UTC) is shown in the inset in Fig. 8. A regression analysis was successfully performed for UCC-IBBCEAS and UAF-CRDS and revealed  $r^2 = 0.948$ , slope = 1.007, offset = 2.1 pptv and  $r^2 = 0.934$ , slope = 0.974, offset = -1.0 pptv, respectively. FZJ-DOAS and ULEIC-BBCRDS allowed no meaningful analysis for this time period because the NO<sub>3</sub> mixing ratios were below or close to the detection limit. ULEIC-BBCRDS measured only in the morning when NO<sub>3</sub> merely varied within  $\pm 2$  pptv, so that the regression line is not well defined.

*20 and 21 June:* The first oxidation experiment of  $\beta$ -pinene with NO<sub>3</sub> was performed in dry air on 20 June. After the  $\beta$ -pinene injection (09:10 UTC) very rapid formation of SOA was observed (cf. Fig. 4). The excellent precision of the CRDS and CEAS instruments allowed us to visualise an increasing systematic difference in the NO<sub>3</sub> mixing ratios relative to the reference technique. The resulting 'u-shaped' scatter plots are presented individually for each instrument by the blue circles in Fig. 6 and compared to each other in the corresponding panel of Fig. 8. This observation is very similar to the experiments on 15 and 16 June described above. The data sets were nevertheless very well ( $r^2 = 0.974 \dots 0.994$ ) correlated with the reference instrument and the slopes of regression

970 close to unity (FZJ-DOAS) or slightly lower (1.01...0.84) except for UCC-IBBCEAS (see Sect. 3.2).  
Details are analysed in Sect. 4.4.2.

On 21 June, the previous experiment was repeated at high relative humidity. The correlation and regression results were fairly similar to 20 June. Coefficients of determination ( $r^2$ ) were close to unity, the intercepts were negligible, and the slopes of FZJ-DOAS, MPI-CRDS, and UAF-CRDS  
975 were nearly identical for both days. The UHD-CEDOAS and ULEIC-BBCRDS instruments both slightly overestimated the  $\text{NO}_3$  mixing ratio (slopes 1.15 and 1.19, respectively). Again data of FZJ-DOAS correlated linearly with the NOAA reference instrument ( $r^2 = 0.966$ , slope = 1.0,  $q = 0.15$ ) as well as the data of UAF-CRDS ( $r^2 = 0.991$ ,  $q = 0.86$ ). However, the measured  $\text{NO}_3$  mixing ratios were the lowest ones of all instruments on both SOA days (slopes were 0.84 on 20 June, and 0.86  
980 on 21 June).

Unfortunately the measurements stopped before the maximum  $\text{NO}_3$  mixing ratio was reached. However, the comparison of the  $\text{NO}_3$  mixing ratios above 70 pptv with the linear regression lines of the MPI-CRDS and UAF-CRDS instruments (violet diamonds and grey circles in the last panel of Fig. 8) clearly showed significantly smaller mixing ratios as would be expected from the regression  
985 (see also 4.4.2). This observation resembled the findings of the previous day. The UHD-CEDOAS instruments measured only few  $\text{NO}_3$  data points on 21 June because of instrumental tests. ULEIC-BBCRDS stopped measurements on 13:30 UTC resulting in an also limited data set during the time when the chamber was loaded with aerosol.

## 4 Discussion

### 990 4.1 Uncertainty of the inlet transmission efficiency of the NOAA-CRDS instrument

The transmission efficiency of NOAA-CRDS determined during NO3Comp was 10 % lower than measured in a post-campaign lab study. However, only few calibrations were made during the campaign due to technical difficulties with the calibration source used at the chamber (see section 2.1.1), thus an additional 10 % uncertainty was added by the authors to account for the calibration problems  
995 during NO3Comp, resulting in a final accuracy of +0.17 / -0.05.

The large data set of the day-to-day correlations of the instruments relative to NOAA-CRDS allows us to apply a statistical test to determine the most likely calibration accuracy of the instrument. The slopes of the linear regressions for clean-air and aerosol-containing air are close to unity. A Chi-square statistic to the 95 % confidence level (NIST/SEMATECH, 20 May 2012) was used to test the  
1000 null hypothesis that the true standard deviation of the slopes is less than the specified value of 0.17. From the table of the critical values of the Chi-Square distribution, the value of  $\chi_{0.95}^2 = 36.42$  had to be compared to the observed value of  $\chi_{exp}^2 = 14.25$ , and consequently the hypothesis has to be accepted. Equality of both  $\chi^2$  values was obtained for a 'true' standard deviation of 0.11. Hence, the analysis indicates that the conservatively estimated upper limit of the accuracy of the NOAA-CRDS

1005 instrument (0.17) is very likely overestimated by 35 %.

#### 4.2 Cross sensitivity to NO<sub>2</sub> - Experiment on 9 June

Generally, the potential interference of NO<sub>2</sub> on the detection of NO<sub>3</sub> is expected to be minor. The optical absorption coefficient of NO<sub>2</sub> in the spectral range of the NO<sub>3</sub> absorption band is small ( $1.27 \times 10^{-4} \times \sigma(\text{NO}_3)$ ). Hence, the resulting interference signal from NO<sub>2</sub> ought to be of minor  
1010 relevance, unless the NO<sub>2</sub> mixing ratio greatly exceeds that of NO<sub>3</sub>. Figure 9 compares the observed differences in NO<sub>3</sub> measurements relative to NOAA-CRDS as a function of NO<sub>2</sub> mixing ratios. NO<sub>3</sub> values below 5 pptv were excluded from this and all following investigations. Circles denote the median, boxes stand for 25 % and 75 % percentiles, and vertical lines are the 10<sup>th</sup> and 90<sup>th</sup> percentiles of the distribution in the particular interval. For none of the data sets a trend could  
1015 be identified. Regression slopes listed in Table 4 are close to unity (0.94 ... 1.04) and intercepts are negligible. MPI-CRDS and ULEIC-BBCRDS did not measure on 9 June.

#### 4.3 Cross sensitivity to H<sub>2</sub>O - Experiment on 10 June

All instruments made use of the strong NO<sub>3</sub>  $B \leftarrow X$  absorption transition centred at 662 nm, which partly overlaps with the spectrally much sharper overtone bands of H<sub>2</sub>O within the  $4\nu + \delta$  polyad  
1020 centred at 652 nm. The impact of the water absorption on the retrieval of NO<sub>3</sub> mixing ratios was therefore investigated in a clean air experiment on 10 June. NO<sub>3</sub> was formed in the flushed dry chamber (water mixing ratio < 100 ppmv) and the water mixing ratio was increased in several steps to 1.1 % (Fig. 3). For instruments using the cavity ring-down principle the effect of water vapour absorption on the detection of NO<sub>3</sub> radicals is small, because the contribution of the water vapour  
1025 absorption is subtracted from the signal by the selective removal of NO<sub>3</sub> in the sample by titration with NO (cf. Eq. (1)). The precondition is, however, that the time interval between zero ring-down measurements is smaller than the time it takes for significant changes of water vapour concentration to occur in the sample, which was the case for NO3Comp. Broad-band CEAS and CRDS instruments as well as DOAS are potentially more severely affected by water vapour absorption (Aliwell and  
1030 Jones, 1996; Platt and Stutz, 2008). Usually the spectral resolution of the instruments used for the measurement of atmospheric NO<sub>3</sub> is not sufficiently high to fully resolve the narrow atmospheric absorption lines of water vapour. This can give rise to apparent non-linearity between the optical density measured and the real atmospheric water concentration if not corrected for by appropriate means (see, for instance, Ball and Jones (2003), Bitter et al. (2005)).

1035 In Fig. 10 the relative differences between the instruments and NOAA-CRDS is plotted in intervals of the water vapour partial pressure in the chamber. Only the UHD-CEDOAS instrument was affected by higher water vapour mixing ratios. As can be seen in Fig. 3 (black squares) UHD-CEDOAS and NOAA-CRDS data agreed as long as the chamber air was dry. With the addition of water vapour an increasing difference between the UHD-CEDOAS data and NOAA-CRDS is ob-

1040 served which levels off at higher partial pressures of water. Simultaneously the size of the error  
bars (not shown) increased from 10 pptv in dry air, to some 30 pptv at the final partial pressure of  
water which indicates a notable influence of water vapour, at least for this experiment. Possibly  
the reduction of the light path due to water vapor was not taken into account properly in the data  
evaluation of this day. FZJ-DOAS, UCC-IBBCEAS, and UAF-CRDS showed no dependency on  
1045 water vapour. The observed scatter of the FZJ-DOAS ratio in Fig. 10 is attributable to instabilities  
of the Xe arc lamps causing 'jumps' of the DOAS data relative to the very precise NOAA-CRDS  
instrument. The offset in the UCC-IBBCEAS data resulted from the missing update of the zero air  
reference spectrum as discussed in Sect. 3.2. The apparent increase of the relative difference of the  
ULEIC-BBCRDS instrument shown in Fig. 10 is not due to a cross interference by water vapour,  
1050 but to inhomogeneities in the sample flow (see Sect. 3.2). We want to point out, that the NO<sub>2</sub> and  
water vapour tests were done early in the campaign, so not all the instruments were yet performing  
optimally.

#### 4.4 Cross sensitivity to aerosol

The comparison of N<sub>2</sub>O<sub>5</sub> measurements during NO<sub>3</sub>Comp by Fuchs et al. (2012) showed that the  
1055 inlet transmission efficiency for N<sub>2</sub>O<sub>5</sub> of some instruments can degrade in the presence of aerosol  
on which N<sub>2</sub>O<sub>5</sub> is taken up. The same observations were described above for NO<sub>3</sub>. The aerosol ex-  
periments during NO<sub>3</sub>Comp were divided into three groups: Ambient aerosol on 11 June, inorganic  
(ammonium sulfate, (NH<sub>4</sub>)<sub>2</sub>SO<sub>4</sub>) aerosol on 15 and 18 June, and secondary organic aerosol (SOA)  
on 16, 20, and 21 June. The potential cross sensitivity to aerosol particles was assessed by investi-  
1060 gating the changes of the differences of NO<sub>3</sub> mixing ratios measured by the instruments relative to  
NOAA-CRDS as a function of the aerosol surface concentration. We expected the NOAA-CRDS  
instrument to be the least affected by wall/inlet losses because of the frequent automatic changing  
of the inlet filter (versus filter change only once per day for other instruments), and because of the  
low operating pressure and fast flow rate and therefore minimum residence time of the air inside the  
1065 instrument. For three experiments the analysis did not lead to statistically significant results.

*11 June:* On this day ambient air was pumped into the chamber using a filter on the cham-  
ber's inlet that removed only coarse mode particles. The peak aerosol surface concentration  $S$  in  
the chamber was very low ( $S_{max} = 1.3 \times 10^7 \text{ nm}^2 \text{ cm}^{-3}$ ) and the dynamic range was fairly small  
( $S_{min} = 0.3 \times 10^7 \text{ nm}^2 \text{ cm}^{-3}$ ). For comparison, during the inorganic aerosol experiment on 15 June  
1070  $S$  was a factor of 30 larger. An analysis of the relative differences of NO<sub>3</sub> mixing ratios as function  
of the aerosol surface concentration showed no discernible dependency of the NO<sub>3</sub> measurements  
for any instrument.

*16 June:* The correlation and regression analysis of the limonene oxidation experiment on 16 June  
already identified (varying) losses of NO<sub>3</sub> inside different instruments and their inlets due to SOA. A  
1075 corresponding Box-Whisker plot, however, gave no conclusive results because of the small dynamic

range of the aerosol surface concentration and the limited SMPS data set.

1080 *18 June:* A similar result as on 11 June was obtained for the isoprene/ammonium sulfate seed aerosol experiment on 18 June. During the short time period of high NO<sub>3</sub> mixing ratios, the aerosol surface concentration was relatively low (only about twice the level of the ambient air day) and changed only marginally ( $0.3\text{-}0.4 \times 10^8 \text{ nm}^2 \text{ cm}^{-3}$ ). Also the regression analysis did not show any evidence of a significant effect of aerosol.

#### 4.4.1 Ammonium sulfate aerosol experiment

On 15 June ammonium sulfate aerosol was added twice to the chamber. The data analysis is presented as Box-Whisker plot in Fig. 11. NO<sub>3</sub> mixing ratios from FZJ-DOAS were offset relative to NOAA-CRDS by +28 pptv and highly variable, so that no trend in FZJ-NOAA difference with aerosol surface area could be quantified. Also for UCC-IBBCEAS and ULEIC-BBCRDS (reduced performance due to variable ingress of ambient air) no clear influence of the increasing aerosol concentration on the detection of NO<sub>3</sub> could be inferred. UHD-CEDOAS showed a slight tendency to an increasing NO<sub>3</sub> deficit at the highest aerosol concentrations but a clear trend could not be identified. The most pronounced NO<sub>3</sub> loss was found in the UAF-CRDS instrument. This instrument used one single filter per day. NO<sub>3</sub> losses increased with increasing aerosol load on the filter. The loss of NO<sub>3</sub> is illustrated in the Box-Whisker plots in Fig. 12 and in the regression plot of Fig. 8 (grey circles, slope 0.86). Fuchs et al. (2012) reported similar observations for the measurements of N<sub>2</sub>O<sub>5</sub> in the presence of ammonium sulfate aerosol during NO<sub>3</sub>Comp. They showed that N<sub>2</sub>O<sub>5</sub> mixing ratios recorded by UAF-CRDS were generally much smaller than those by NOAA-CRDS, and concluded, that an unaccounted NO<sub>3</sub> loss in the inlet of the UAF-CRDS instrument might have been the reason. This hypothesis is consistent with the NO<sub>3</sub> measurements.

#### 4.4.2 Secondary Organic Aerosol experiments

As shown in Sect. 3.3.3 several instruments clearly detected lower NO<sub>3</sub> mixing ratios than the NOAA-CRDS instrument after secondary organic aerosol was formed in the reaction of  $\beta$ -pinene with NO<sub>3</sub> in dry air on 20 June (cf. Fig. 8 and Fig. 6 - blue circles). The Box-Whisker plots in Fig. 12 present the difference of NO<sub>3</sub> mixing ratios relative to NOAA-CRDS as function of the measured dry SOA surface concentration. Note, in contrast to the experiment on 15 June the aerosol concentration was highest in the beginning of the experiment and decreased towards the end, so that the integrated 'aerosol exposure' increases from right to left in Fig. 12. As discussed in Sect. 3.3.3 the DOAS based techniques FZJ-DOAS and UHD-CEDOAS were mostly unaffected by aerosol. For the remaining instruments (using no or just a single filter per day) a clear trend to lower NO<sub>3</sub> mixing ratios relative to NOAA was evident which is consistent with the hypothesis that NO<sub>3</sub> is partially removed from sample air as it is drawn through the inlet and filters which are covered with reactive organic aerosol. Fry et al. (2009) investigated the chemistry and the SOA yield for this chamber

experiment using a gas-phase kinetics/aerosol partitioning model. They found an unexplained high yield of 6 ppbv of HNO<sub>3</sub> at the end of the dry β-pinene experiment which they attributed to heterogeneous reaction of NO<sub>3</sub> on organic aerosol surfaces, abstracting H from an alkane. This type of reaction could also be responsible for the partial loss of NO<sub>3</sub> in the inlet systems of the instruments.

1115 In this context we note that Tang et al. (2010) have shown that filter losses of NO<sub>3</sub> and N<sub>2</sub>O<sub>5</sub> can be very variable, with contamination by ambient aerosol containing organic compounds strongly favouring NO<sub>3</sub> loss.

A corresponding Box-Whisker analysis could not be performed for the experiment on 21 June which repeated the measurements of the previous day at high relative humidity. Shortly after the  
1120 maximum aerosol surface concentration was reached, a technical issue caused the SMPS to stop measuring, leaving too few data per bin for a convincing analysis. Fry et al. (2009) showed that both experiments did not significantly differ in terms of reaction mechanism and aerosol yields. However, due to the five-fold higher wall losses of NO<sub>3</sub> (and N<sub>2</sub>O<sub>5</sub>) at 60 % RH (Fry et al., 2009) but comparable NO<sub>3</sub> production rates for both experiments, the NO<sub>3</sub> (and N<sub>2</sub>O<sub>5</sub>) mixing ratios were  
1125 significantly lower on 21 June. Consequently the maximum of the aerosol surface concentration was reached about 45 min later compared to the dry experiment and also the formation of HNO<sub>3</sub> was limited to only 2.5 ppbv. However, the temporal profiles of the NO<sub>3</sub> mixing ratios on both days were very similar showing increasing differences of NO<sub>3</sub> between the instruments towards the end of the measurements (Sect. 3.3.3 and Fig. 4).

1130 So far, it is not understood why the UCC-IBBCEAS instrument, which detected NO<sub>3</sub> in situ in the chamber, showed the identical behaviour on 20 June as the instruments using inlet lines and aerosol filters. Contrary to UCC-IBBCEAS, both other in situ techniques, FZJ-DOAS and UHD-CEDOAS, were unaffected by aerosol as can be seen in the corresponding panels in Fig. 6 (blue circles). Their NO<sub>3</sub> data scatter uniformly around the regression lines. It is unlikely that the observed effects  
1135 resulted from a feature of the NOAA-CRDS reference instrument. Filters were exchanged frequently at short time intervals during the aerosol experiments. The fact that the temporal profiles of the NO<sub>3</sub> mixing ratios did not show any discontinuities between filter changes was convincingly verified. This is in contrast to the MPI-CRDS instrument which changed the filter rarely and therefore is more vulnerable for losses of NO<sub>3</sub>. An example for NO<sub>3</sub> losses on the surface of a filter is shown  
1140 in the temporal profile of the NO<sub>3</sub> mixing ratios on 20 June (solid violet diamonds in Fig. 4). At 13:30 UTC, close to the maximum of the NO<sub>3</sub> mixing ratio, the aerosol filter of the MPI-CRDS instrument was exchanged. After restarting the measurements the difference in the NO<sub>3</sub> mixing ratio relative to NOAA-CRDS was considerably smaller than before the filter change.

## 5 Summary and Conclusions

1145 Instruments developed for the detection of tropospheric  $\text{NO}_3$  radicals were compared during the  
'NO3Comp' campaign. Simultaneous measurements of  $\text{NO}_3$  radical mixing ratios were conducted  
by seven instruments under well controlled experimental conditions at the atmosphere simulation  
chamber SAPHIR in Jülich. All  $\text{NO}_3$  instruments assembled at the chamber were based on absorp-  
tion spectroscopy. Four instruments made use of the principle of cavity ring-down spectroscopy, two  
1150 utilised cavity enhanced absorption spectroscopy, and one applied 'classical' differential optical ab-  
sorption spectroscopy. The latter three instruments detected  $\text{NO}_3$  in situ in open-path configuration  
inside the chamber, while the CRDS instruments extracted air from the well mixed chamber volume.  
On twelve days in June 2007 chamber studies were performed under a wide variety of chemical con-  
ditions. The experiments were designed to compare the instruments under variable concentrations  
1155 of  $\text{NO}_3$ ,  $\text{N}_2\text{O}_5$ ,  $\text{NO}_2$ , and water vapour, in the presence of inorganic aerosol injected into the cham-  
ber or during complex experiments investigating the oxidation of terpenes with  $\text{NO}_3$  accompanied  
by formation of secondary organic aerosol, but also for mixing ratio conditions representative of  
ambient atmosphere.

Zero air measurements in the clean chamber were used to study the precision of the  $\text{NO}_3$  detec-  
1160 tion. The overall precision of the IBBCEAS and the CRDS instruments varied within 0.5 and 2 pptv,  
that of the CEDOAS and the DOAS instrument was 5 pptv and 9 pptv, respectively. The instrumental  
'zero' was also very well defined. The maximum deviation was  $\pm 0.2$  pptv for the IBBCEAS and  
the CRDS instruments and +3 pptv and +2 pptv for the CEDOAS and the DOAS instrument, respec-  
tively. The sensitivity of the cavity assisted techniques was very high and permitted the detection  
1165 of  $\text{NO}_3$  radicals with the precision stated above with a time resolution of 1 s (NOAA-CRDS and  
UAF-CRDS), 5 s (UCC-CEAS), 10 s (MPI-CRDS), 1 min (ULEIC-BBCRDS and FZJ-DOAS), and  
5 min (UHD-CEDOAS).

Overall, in situ instruments (FZJ-DOAS, UCC-IBBCEAS, and UHD-CEDOAS) are in very good  
agreement with instruments sampling air from the chamber volume. The  $\text{NO}_3$  data of all instruments  
1170 are very well linearly correlated with the NOAA-CRDS instrument which was selected as the com-  
mon reference to compare the instruments. The median of the coefficient of determination,  $r^2$ , for all  
experiment days (60 correlations) is  $r^2 = 0.981$  (1./3. quartile = 0.949/0.994; min/max = 0.540/0.999,  
cf. Tab. 4). The linear regression analysis of the corresponding data set yielded very small intercepts  
( $1.2 \pm 5.3$  pptv, min -14 pptv, max +22 pptv) and the average slope of the regression lines was close  
1175 to unity ( $1.02 \pm 0.13$ ; min 0.72, max 1.36). In any case the deviation of the individual regression  
slopes from unity was within the combined accuracies of the instrument pairs compared. The vari-  
ety of  $\text{NO}_3$  instruments, their exceptionally high precision and accuracy, the large dynamic range  
of the  $\text{NO}_3$  measurements, and the comprehensive set of  $\text{NO}_3$  data acquired under the well con-  
trolled homogeneous measurement conditions in the atmosphere simulation chamber allowed the  
1180 performance of a rigorous statistical data analysis which would not have been possible under less

controlled conditions as e.g. encountered in field campaigns.

No hint for a cross interference of  $\text{NO}_2$  was found for the instruments. The effect of non-Lambert-Beer behaviour of water vapour absorption lines on the accuracy of the  $\text{NO}_3$  detection by broadband CEAS and DOAS was found to be small and well accounted for in the data products supplied by the  
1185 instrument operators.

The loss of  $\text{NO}_3$  in the air sampling inlet systems of the instruments which sampled air from the chamber had to be accurately measured. Correction factors under very different chemical conditions were experimentally determined by the participants during NO3Comp and applied for their respective data retrieval. The very good correspondence between the time-dependent  $\text{NO}_3$  mixing  
1190 ratios measured by all instruments for all aerosol-free experiments indicated that the inlet losses were generally quantified reliably. For experiments with aerosol loading on the inlet systems, however, a marked difference in the loss of  $\text{NO}_3$  was noted between instruments using no or just a single aerosol filter per day, and the NOAA-CRDS reference instrument in which the filter was replaced regularly. Differences between  $\text{NO}_3$  data were detectable in experiments with added inorganic aerosol or SOA  
1195 formed during the experiment. The discrepancies increased with time, pointing to accumulating losses due to high aerosol loadings. No difference was found for losses of  $\text{NO}_3$  on inorganic or organic aerosol particles. Instruments using DOAS-type analysis showed no significant effect of aerosol on the detection of  $\text{NO}_3$ .

The NO3Comp campaign demonstrated the high quality, reliability, and robustness of performance of current state-of-the-art instrumentation for  $\text{NO}_3$  detection. It was shown that the most  
1200 significant influence on the performance of instruments was generally caused by the presence of aerosol. Consequently instruments deployed to field measurements concerning  $\text{NO}_3$  (and  $\text{N}_2\text{O}_5$ ) need to filter the sample air from aerosol particles by Teflon filters close to the head of the sampling line. The filters should be exchanged frequently depending on the aerosol loading of the air.  
1205 There is no general recommendation for the 'lifetime' of the filters. The optimum operating conditions and the inlet losses need to be characterised rigorously and individually for each instrument. The informal NO3Comp intercomparison stimulated the exchange of ideas and methodologies for tropospheric  $\text{NO}_3$  and  $\text{N}_2\text{O}_5$  detection and was very helpful for the further development of these instruments. Their employment on different platforms in the field is ongoing.

1210 *Acknowledgements.* The authors thank Robert Wegener for measurement of butanal concentrations shown in Fig. 3. The NO3Comp campaign was supported by the European Community funded Network of Excellence ACCENT - Atmospheric Composition Change: the European Network (Grant GOCE-CT-2004-505337) and the FP-6 programme Support for Research Infrastructures: Integrated Infrastructure Initiative: EUROCHAMP (Grant RII3-CT-2004-505968). Authors associated with University of Alaska Fairbanks were supported by  
1215 the National Science Foundation (Grants CHE- 0094038 and ATM-0624448), as well as by the United States Department of Energy (Grant DE-FG02-03ER83695). The UCC team acknowledges support from the Irish Environmental Protection Agency (Project: TRACES 2005-ET-MS-28-M3). The University of Leicester authors acknowledge support from the Natural Environment Research Council via a PhD studentship for Alex Shillings and a grant (NER/T/S/2002/00036) to develop the BBCRDS instrument.

## 1220 **References**

- Aldener, M., Brown, S. S., Stark, H., Williams, E. J., Lerner, B. M., Kuster, W. C., Goldan, P. D., Quinn, P. K., Bates, T. S., Fehsenfeld, F. C., and Ravishankara, A. R.: Reactivity and loss mechanisms of NO<sub>3</sub> and N<sub>2</sub>O<sub>5</sub> in a polluted marine environment: Results from in situ measurements during New England Air Quality Study 2002, *J. Geophys. Res.*, 111, D23s73, doi:10.1029/2006jd007252, 2006.
- 1225 Aliwell, S. R. and Jones, R. L.: Measurement of atmospheric NO<sub>3</sub>. I. Improved removal of water vapour absorption features in the analysis for NO<sub>3</sub>, *Geophys. Res. Lett.*, 23, 2585–2588, 1996.
- Allan, B. J., McFiggans, G., Plane, J. M. C., Coe, H., and McFadyen, G. G.: The nitrate radical in the remote marine boundary layer, *J. Geophys. Res.*, 105, 24 191–24 204, 2000.
- Ayers, J. D., Apodaca, R. L., Simpson, W. R., and Baer, D. S.: Off-axis cavity ringdown spectroscopy: application to atmospheric nitrate radical detection, *Appl. Opt.*, 44, 7239–7242, 2005.
- 1230 Ball, S. M. and Jones, A. E.: *Broadband Cavity Ring-Down Spectroscopy*, chap. 3, pp. 57–88, John Wiley and Sons, 2009.
- Ball, S. M. and Jones, R. L.: Broad-band cavity ring-down spectroscopy, *Chem. Rev.*, 103, 5239–5262, 2003.
- Bitter, M., Ball, S. M., Povey, I. M., and Jones, R. L.: A broadband cavity ringdown spectrometer for in-situ measurements of atmospheric trace gases, *Atmos. Chem. Phys.*, 5, 2547–2560, 2005.
- 1235 Bossmeyer, J., Brauers, T., Richter, C., Rohrer, F., Wegener, R., and Wahner, A.: Simulation chamber studies on the NO<sub>3</sub> chemistry of atmospheric aldehydes, *Geophys. Res. Lett.*, 33, L18 810, doi:10.1029/2006gl026778, 2006.
- Brauers, T., Bossmeyer, J., Dorn, H.-P., Schlosser, E., Tillmann, R., Wegener, R., and Wahner, A.: Investigation of the formaldehyde differential absorption cross section at high and low spectral resolution in the simulation chamber SAPHIR, *Atmos. Chem. Phys.*, 7, 3579–3586, 2007.
- 1240 Brown, S. S.: Absorption spectroscopy in high-finesse cavities for atmospheric studies, *Chem. Rev.*, 103, 5219–5238, doi:10.1021/cr020645c, 2003.
- Brown, S. S. and Stutz, J.: Nighttime radical observations and chemistry, *Chemical Society Reviews*, 41, 6405–6447, doi:10.1039/c2cs35181a, 2012.
- 1245 Brown, S. S., Stark, H., Ciciora, S. J., and Ravishankara, A. R.: In-situ measurement of atmospheric NO<sub>3</sub> and N<sub>2</sub>O<sub>5</sub> via cavity ring-down spectroscopy, *Geophys. Res. Lett.*, 28, 3227–3230, 2001.
- Brown, S. S., Stark, H., Ciciora, S. J., McLaughlin, R. J., and Ravishankara, A. R.: Simultaneous in situ detection of atmospheric NO<sub>3</sub> and N<sub>2</sub>O<sub>5</sub> via cavity ring-down spectroscopy, *Rev. Sci. Instrum.*, 73, 3291–3301, doi:10.1063/1.1499214, 2002a.
- 1250 Brown, S. S., Stark, H., and Ravishankara, A. R.: Cavity ring-down spectroscopy for atmospheric trace gas detection: application to the nitrate radical (NO<sub>3</sub>), *Appl. Phys. B*, 75, 173–182, doi:10.1007/s00340-002-0980-y, 2002b.
- Brown, S. S., Stark, H., Ryerson, T. B., Williams, E. J., Nicks, D. K., Trainer, M., Fehsenfeld, F. C., and Ravishankara, A. R.: Nitrogen oxides in the nocturnal boundary layer: Simultaneous in situ measurements of NO<sub>3</sub>, N<sub>2</sub>O<sub>5</sub>, NO<sub>2</sub>, NO, and O<sub>3</sub>, *J. Geophys. Res.*, 108, 4299, doi:10.1029/2002jd002917, 2003.
- 1255 Brown, S. S., Dibb, J. E., Stark, H., Aldener, M., Vozella, M., Whitlow, S., Williams, E. J., Lerner, B. M., Jakoubek, R., Middlebrook, A. M., DeGouw, J. A., Warneke, C., Goldan, P. D., Kuster, W. C., Angevine, W. M., Sueper, D. T., Quinn, P. K., Bates, T. S., Meagher, J. F., Fehsenfeld, F. C., and Ravishankara, A. R.:

- 1260 Nighttime removal of NO<sub>x</sub> in the summer marine boundary layer, *Geophys. Res. Lett.*, 31, L07 108, doi: 10.1029/2004gl019412, 2004.
- Brown, S. S., Osthoff, H. D., Stark, H., Dubé, W. P., Ryerson, T. B., Warneke, C., de Gouw, J. A., Wollny, A. G., Parrish, D. D., Fehsenfeld, F. C., and Ravishankara, A. R.: Aircraft observations of daytime NO<sub>3</sub> and N<sub>2</sub>O<sub>5</sub> and their implications for tropospheric chemistry, *J. Photochem. Photobiol., A*, 176, 270–278, doi:10.1016/j.jphotochem.2005.10.004, 2005.
- 1265 Brown, S. S., Neuman, J. A., Ryerson, T. B., Trainer, M., Dubé, W. P., Holloway, J. S., Warneke, C., de Gouw, J. A., Donnelly, S. G., Atlas, E., Matthew, B., Middlebrook, A. M., Peltier, R., Weber, R. J., Stohl, A., Meagher, J. F., Fehsenfeld, F. C., and Ravishankara, A. R.: Nocturnal odd-oxygen budget and its implications for ozone loss in the lower troposphere, *Geophys. Res. Lett.*, 33, L08 801, 2006.
- 1270 Brown, S. S., Dubé, W. P., Osthoff, H. D., Wolfe, D. E., Angevine, W. M., and Ravishankara, A. R.: High resolution vertical distributions of NO<sub>3</sub> and N<sub>2</sub>O<sub>5</sub> through the nocturnal boundary layer, *Atmos. Chem. Phys.*, 7, 139–149, 2007.
- Canagaratna, M. R., Jayne, J. T., Jimenez, J. L., Allan, J. D., Alfarra, M. R., Zhang, Q., Onasch, T. B., Drewnick, F., Coe, H., Middlebrook, A., Delia, A., Williams, L. R., Trimborn, A. M., Northway, M. J., DeCarlo, P. F., Kolb, C. E., Davidovits, P., and Worsnop, D. R.: Chemical and microphysical characterization of ambient aerosols with the aerodyne aerosol mass spectrometer, *Mass Spectrometry Reviews*, 26, 185–222, doi:10.1002/Mas.20115, 2007.
- 1275 Chang, W. L., Bhave, P. V., Brown, S. S., Riemer, N., Stutz, J., and Dabdub, D.: Heterogeneous Atmospheric Chemistry, Ambient Measurements, and Model Calculations of N(2)O(5): A Review, *Aerosol Sci. Technol.*, 45, 665–695, doi:10.1080/02786826.2010.551672, 2011.
- 1280 Doussin, J.-F., Dominique, R., and Patrick, C.: Multiple-Pass Cell for Very-Long-Path Infrared Spectrometry, *Appl. Opt.*, 38, 4145–4150, doi:10.1364/AO.38.004145, 1999.
- Dubé, W. P., Brown, S. S., Osthoff, H. D., Nunley, M. R., Ciciora, S. J., Paris, M. W., McLaughlin, R. J., and Ravishankara, A. R.: Aircraft instrument for simultaneous, in situ measurement of NO<sub>3</sub> and N<sub>2</sub>O<sub>5</sub> via pulsed cavity ring-down spectroscopy, *Rev. Sci. Instrum.*, 77, 034 101, doi:10.1063/1.2176058, 2006.
- 1285 Efron, B. and Tibshirani, R. J.: *An Introduction to the Bootstrap*, Chapman and Hall, New York, 1993.
- Fiedler, S. E., Hese, A., and Ruth, A. A.: Incoherent broad-band cavity-enhanced absorption spectroscopy, *Chem. Phys. Lett.*, 371, 284–294, doi:10.1016/j.cplett.2003.10.075, 2003.
- Fiedler, S. E., Hese, A., and Ruth, A. A.: Incoherent broad-band cavity-enhanced absorption spectroscopy of liquids, *Rev. Sci. Instrum.*, 76, 023 107, doi:10.1063/1.1841872, 2005.
- 1290 Fiedler, S. E., Hese, A., and Heitmann, U.: Influence of the cavity parameters on the output intensity in incoherent broadband cavity-enhanced absorption spectroscopy, *Rev. Sci. Instrum.*, 78, 073 104, doi: 10.1063/1.2752608, 2007.
- Freedman, D. and Diaconis, P.: On the histogram as a density estimator: L<sub>2</sub> Theory, *Probability Theory and Related Fields*, 57, 453–476, doi:10.1007/bf01025868, 1981.
- 1295 Fry, J. L., Kiendler-Scharr, A., Rollins, A. W., Wooldridge, P. J., Brown, S. S., Fuchs, H., Dubé, W., Mensah, A., dal Maso, M., Tillmann, R., Dorn, H.-P., Brauers, T., and Cohen, R. C.: Organic nitrate and secondary organic aerosol yield from NO<sub>3</sub> oxidation of  $\beta$ -pinene evaluated using a gas-phase kinetics/aerosol partitioning model, *Atmos. Chem. Phys.*, 9, 1431–1449, doi:10.5194/acp-9-1431-2009, 2009.

- 1300 Fry, J. L., Kiendler-Scharr, A., Rollins, A. W., Brauers, T., Brown, S. S., Dorn, H.-P., Dubé, W. P., Fuchs, H., Mensah, A., Rohrer, F., Tillmann, R., Wahner, A., Wooldridge, P. J., and Cohen, R. C.: SOA from limonene: role of NO<sub>3</sub> in its generation and degradation, *Atmos. Chem. Phys.*, 11, 3879–3894, doi:10.5194/acp-11-3879-2011, 2011.
- Fuchs, H., Dubé, W. P., Ciciora, S. J., and Brown, S. S.: Determination of Inlet Transmission and Conversion
- 1305 Efficiencies for in Situ Measurements of the Nocturnal Nitrogen Oxides, NO<sub>3</sub>, N<sub>2</sub>O<sub>5</sub> and NO<sub>2</sub>, via Pulsed Cavity Ring-Down Spectroscopy, *Anal. Chem.*, 80, 6010–6017, doi:10.1021/ac8007253, 2008.
- Fuchs, H., Ball, S. M., Bohn, B., Brauers, T., Cohen, R. C., Dorn, H.-P., Dubé, W. P., Fry, J. L., Häsel, R., Heitmann, U., Jones, R. L., Kleffmann, J., Mentel, T. F., Müsgen, P., Rohrer, F., Rollins, A. W., Ruth, A. A., Kiendler-Scharr, A., Schlosser, E., Shillings, A. J. L., Tillmann, R., Varma, R. M., Venables, D. S.,
- 1310 Villena Tapia, G., Wahner, A., Wegener, R., Wooldridge, P. J., and Brown, S. S.: Intercomparison of measurements of NO<sub>2</sub> concentrations in the atmosphere simulation chamber SAPHIR during the NO<sub>3</sub>Comp campaign, *Atmos. Meas. Tech.*, 3, 21–37, doi:10.5194/amt-3-21-2010, 2010a.
- Fuchs, H., Brauers, T., Dorn, H.-P., Harder, H., Haeseler, R., Hofzumahaus, A., Holland, F., Kanaya, Y., Kajii, Y., Kubistin, D., Lou, S., Martinez, M., Miyamoto, K., Nishida, S., Rudolf, M., Schlosser, E., Wahner, A., Yoshino, A., and Schurath, U.: Technical Note: Formal blind intercomparison of HO<sub>2</sub> measurements
- 1315 in the atmosphere simulation chamber SAPHIR during the HO<sub>x</sub>Comp campaign, *Atmos. Chem. Phys.*, 10, 12 233–12 250, doi:10.5194/acp-10-12233-2010, 2010b.
- Fuchs, H., Simpson, W. R., Apodaca, R. L., Brauers, T., Cohen, R. C., Crowley, J. N., Dorn, H.-P., Dubé, W. P., Fry, J. L., Häsel, R., Kajii, Y., Kiendler-Scharr, A., Labazan, I., Matsumoto, J., Mentel, T. F., Nakashima, Y., Rohrer, F., Rollins, A. W., Schuster, G., Tillmann, R., Wahner, A., Wooldridge, P. J., and Brown, S. S.: Comparison of N<sub>2</sub>O<sub>5</sub> mixing ratios during NO<sub>3</sub>Comp 2007 in SAPHIR, *Atmos. Meas. Tech.*, 5, 2763–2777, doi:10.5194/amt-5-2763-2012, 2012.
- Geyer, A., Alicke, B., Mihelcic, D., Stutz, J., and Platt, U.: Comparison of tropospheric NO<sub>3</sub> radical measurements by differential optical absorption spectroscopy and matrix isolation electron spin resonance, *J. Geophys. Res.*, 104, 26 097–26 105, 1999.
- 1325 Geyer, A., Ackermann, R., Dubois, R., Lohrmann, B., Müller, T., and Platt, U.: Long-term observation of nitrate radicals in the continental boundary layer near Berlin, *Atmos. Environ.*, 35, 3619–3631, doi:10.1016/S1352-2310(00)00549-5, 2001.
- Geyer, A., Alicke, B., Ackermann, R., Martinez, M., Harder, H., Brune, W., di Carlo, P., Williams, E., Jobson, T., Hall, S., Shetter, R., and Stutz, J.: Direct observations of daytime NO<sub>3</sub>: Implications for urban boundary layer chemistry, *J. Geophys. Res.*, 108, 4368, doi:10.1029/2002jd002967, 2003.
- 1330 Gherman, T., Venables, D. S., Vaughan, S., Orphal, J., and Ruth, A. A.: Incoherent broadband cavity-enhanced absorption spectroscopy in the near-ultraviolet: Application to HONO and NO<sub>2</sub>, *Environ. Sci. Technol.*, 42, 890–895, doi:10.1021/es0716913|ISSN0013-936X, 2008.
- 1335 Hausmann, M., Brandenburger, U., Brauers, T., and Dorn, H.-P.: Simple Monte Carlo methods to estimate the spectra evaluation error in differential-optical-absorption spectroscopy, *Appl. Opt.*, 38, 462–475, doi:10.1364/AO.38.000462, 1999.
- Kasyutich, V. L., Canosa-Mas, C. E., Pfrang, C., Vaughan, S., and Wayne, R. P.: Off-axis continuous-wave cavity-enhanced absorption spectroscopy of narrow-band and broadband absorbers using red diode lasers,

- 1340 Appl. Phys. B, 75, 755–761, 2002.
- King, M. D., Dick, E. M., and Simpson, W. R.: A new method for the atmospheric detection of the nitrate radical (NO<sub>3</sub>), *Atmos. Environ.*, 34, 685–688, doi:10.1016/S1352-2310(99)00418-5, 2000.
- Kraus, S. G.: DOASIS, A Framework Design for DOAS, Dissertation, Institut of Physics, University of Mannheim, Germany, 2006.
- 1345 Langridge, J. M., Ball, S. M., Shillings, A. J. L., and Jones, R. L.: A broadband absorption spectrometer using light emitting diodes for ultrasensitive, in situ trace gas detection, *Rev. Sci. Instrum.*, 79, 123 110–14, doi:10.1063/1.3046282, 2008a.
- Langridge, J. M., Laurila, T., Watt, R. S., Jones, R. L., Kaminski, C. F., and Hult, J.: Cavity enhanced absorption spectroscopy of multiple trace gas species using a supercontinuum radiation source, *Opt. Express*, 16, 10 178–10 188, doi:10.1364/OE.16.010178, 2008b.
- 1350 Lindinger, W., Hansel, A., and Jordan, A.: On-line monitoring of volatile organic compounds at pptv levels by means of proton-transfer-reaction mass spectrometry (PTR-MS) - Medical applications, food control and environmental research, *Int. J. Mass Spectrom.*, 173, 191–241, doi:10.1016/S0168-1176(97)00281-4, 1998.
- Matsumoto, J., Kosugi, N., Imai, H., and Kajii, Y.: Development of a measurement system for nitrate radical and dinitrogen pentoxide using a thermal conversion/laser-induced fluorescence technique, *Rev. Sci. Instrum.*, 76, 064 101, doi:10.1063/1.1927098, 2005.
- 1355 McLaren, R., Salmon, R. A., Liggio, J., Hayden, K. L., Anlauf, K. G., and Leitch, W. R.: Nighttime chemistry at a rural site in the Lower Fraser Valley, *Atmos. Environ.*, 38, 5837–5848, doi:10.1016/j.atmosenv.2004.03.074, 2004.
- 1360 Meinen, J., Thieser, J., Platt, U., and Leisner, T.: Technical Note: Using a high finesse optical resonator to provide a long light path for differential optical absorption spectroscopy: CE-DOAS, *Atmos. Chem. Phys.*, 10, 3901–3914, doi:10.5194/acp-10-3901-2010, 2010.
- Mihelcic, D., Klemp, D., Musgen, P., Patz, H. W., and Volzthomas, A.: Simultaneous Measurements of Peroxy and Nitrate Radicals at Schauinsland, *J. Atmos. Chem.*, 16, 313–335, doi:10.1007/BF01032628, 1993.
- 1365 NIST/SEMATECH: e-Handbook of Statistical Methods, <http://www.itl.nist.gov/div898/handbook/>, 20 May 2012.
- Orphal, J., Fellows, C. E., and Flaud, P. M.: The visible absorption spectrum of NO<sub>3</sub> measured by high-resolution Fourier transform spectroscopy, *J. Geophys. Res.*, 108, D002 489, doi:10.1029/2002JD002489, 2003.
- 1370 Osthoff, H. D., Brown, S. S., Ryerson, T. B., Fortin, T. J., Lerner, B. M., Williams, E. J., Pettersson, A., Baynard, T., Dubé, W. P., Ciciora, S. J., and Ravishankara, A. R.: Measurement of atmospheric NO<sub>2</sub> by pulsed cavity ring-down spectroscopy, *J. Geophys. Res.*, 111, D12 305, doi:10.1029/2005jd006942, 2006.
- Osthoff, H. D., Pilling, M. J., Ravishankara, A. R., and Brown, S. S.: Temperature dependence of the NO<sub>3</sub> absorption cross-section above 298 K and determination of the equilibrium constant for NO<sub>3</sub>+NO<sub>2</sub> ↔ N<sub>2</sub>O<sub>5</sub> at atmospherically relevant conditions, *Phys. Chem. Chem. Phys.*, 9, 5785–5793, doi:10.1039/B709193a, 2007.
- 1375 Paul, J. B., Lapson, L., and Anderson, J. G.: Ultrasensitive absorption spectroscopy with a high-finesse optical cavity and off-axis alignment, *Appl. Opt.*, 40, 4904–4910, 2001.
- Platt, U. and Perner, D.: Direct Measurements of Atmospheric CH<sub>2</sub>O, HNO<sub>2</sub>, O<sub>3</sub>, NO<sub>2</sub>, and SO<sub>2</sub> by Differen-

- 1380 tial Optical Absorption in the Near UV, *J. Geophys. Res.*, 85, 7453–7458, 1980.
- Platt, U. and Stutz, J.: Differential Optical Absorption Spectroscopy - Principles and Applications, *Physics of Earth and Space Environments*, Springer Verlag, Berlin, Heidelberg, 2008.
- Platt, U., Perner, D., Winer, A. M., Harris, G. W., and Pitts, J. N.: Detection of NO<sub>3</sub> in the Polluted Troposphere by Differential Optical-Absorption, *Geophys. Res. Lett.*, 7, 89–92, 1980.
- 1385 Platt, U., Perner, D., Schroder, J., Kessler, C., and Toennissen, A.: The Diurnal-Variation of NO<sub>3</sub>, *J. Geophys. Res.*, 86, 1965–1970, 1981.
- Platt, U., Meinen, J., Pöhler, D., and Leisner, T.: Broadband Cavity Enhanced Differential Optical Absorption Spectroscopy (CE-DOAS) - applicability and corrections, *Atmos. Meas. Tech.*, 2, 713–723, 2009.
- Press, W. H., Teukolsky, S. A., Vetterling, W. T., and Flannery, B. P.: Numerical recipes in C. *The Art of*
- 1390 *Scientific Computing*. 2nd edition, Cambridge University Press, 1992.
- Rohrer, F., Bohn, B., Brauers, T., Brüning, D., Johnen, F.-J., Wahner, A., and Kleffmann, J.: Characterisation of the photolytic HONO-source in the atmosphere simulation chamber SAPHIR, *Atmos. Chem. Phys.*, 5, 2189–2201, 2005.
- Rollins, A. W., Kiendler-Scharr, A., Fry, J. L., Brauers, T., Brown, S. S., Dorn, H.-P., Dubé, W. P., Fuchs,
- 1395 H., Mensah, A., Mentel, T. F., Rohrer, F., Tillmann, R., Wegener, R., Wooldridge, P. J., and Cohen, R. C.: Isoprene oxidation by nitrate radical: alkyl nitrate and secondary organic aerosol yields, *Atmos. Chem. Phys.*, 9, 6685–6703, 2009.
- Sander, S. P., Abbat, J., Barker, R., Burkholder, J. B., Friedl, R. R., Golden, D. M., Huie, R. E., Kolb, C. E., Kurylo, M. J., Moortgat, G. K., Orkin, V. L., and Wine, P.: *Chemical Kinetics and Photochemical Data for Use in Atmospheric Studies*. Evaluation Number 17, JPL Publication 10-6, Jet Propulsion Laboratory, Pasadena, 2011.
- 1400 Schlosser, E., Bohn, B., Brauers, T., Dorn, H.-P., Fuchs, H., Hseler, R., Hofzumahaus, A., Holland, F., Rohrer, F., Rupp, L., Siese, M., Tillmann, R., and Wahner, A.: Intercomparison of two hydroxyl radical measurement techniques at the Atmosphere Simulation Chamber SAPHIR, *J. Atmos. Chem.*, 56, 187–205, doi:10.1007/s10874-006-9049-3, 2007.
- 1405 Schlosser, E., Brauers, T., Dorn, H.-P., Fuchs, H., Häsel, R., Hofzumahaus, A., Holland, F., Wahner, A., Kanaya, Y., Kajii, Y., Miyamoto, K., Nishida, S., Watanabe, K., Yoshino, A., Kubistin, D., Martinez, M., Rudolf, M., Harder, H., Berresheim, H., Elste, T., Plass-Dülmer, C., Stange, G., and Schurath, U.: Technical Note: Formal blind intercomparison of OH measurements: results from the international campaign HOxComp, *Atmos. Chem. Phys.*, 9, 7923–7948, 2009.
- 1410 Schuster, G., Labazan, I., and Crowley, J. N.: A cavity ring down/cavity enhanced absorption device for measurement of ambient NO<sub>3</sub> and N<sub>2</sub>O<sub>5</sub>, *Atmos. Meas. Tech.*, 2, 1–13, 2009.
- Shillings, A. J. L., Ball, S. M., Barber, M. J., Tennyson, J., and Jones, R. L.: An upper limit for water dimer absorption in the 750 nm spectral region and a revised water line list, *Atmos. Chem. Phys.*, 11, 4273–4287, doi:10.5194/acp-11-4273-2011, 2011.
- 1415 Simpson, W. R.: Continuous wave cavity ring-down spectroscopy applied to in situ detection of dinitrogen pentoxide (N<sub>2</sub>O<sub>5</sub>), *Rev. Sci. Instrum.*, 74, 3442–3452, 2003.
- Sommariva, R., Pilling, M. J., Bloss, W. J., Heard, D. E., Lee, J. D., Fleming, Z. L., Monks, P. S., Plane, J. M. C., Saiz-Lopez, A., Ball, S. M., Bitter, M., Jones, R. L., Brough, N., Penkett, S. A., Hopkins, J. R., Lewis, A. C.,

- 1420 and Read, K. A.: Night-time radical chemistry during the NAMBLEX campaign, *Atmos. Chem. Phys.*, 7, 587–598, 2007.
- Stutz, J., Alicke, B., Ackermann, R., Geyer, A., White, A., and Williams, E.: Vertical profiles of NO<sub>3</sub>, N<sub>2</sub>O<sub>5</sub>, O<sub>3</sub>, and NO<sub>x</sub> in the nocturnal boundary layer: 1. Observations during the Texas Air Quality Study 2000, *J. Geophys. Res.*, 109, D12 306, doi:10.1029/2003jd004209, 2004.
- 1425 Tang, M. J., Thieser, J., Schuster, G., and Crowley, J. N.: Uptake of NO<sub>3</sub> and N<sub>2</sub>O<sub>5</sub> to Saharan dust, ambient urban aerosol and soot: a relative rate study, *Atmos. Chem. Phys.*, 10, 2965–2974, 2010.
- Triki, M., Cermak, P., Mejean, G., and Romanini, D.: Cavity-enhanced absorption spectroscopy with a red LED source for NO<sub>x</sub> trace analysis, *Appl. Phys. B*, 91, 195–201, doi:10.1007/s00340-008-2958-x, 2008.
- Troutman, B. M. and Williams, G. P.: *Fitting Straight Lines in the Earth Sciences*, vol. 1, pp. 107–128, Oxford University Press, Oxford, 1987.
- 1430 Varma, R. M., Venables, D. S., Ruth, A. A., Heitmann, U., Schlosser, E., and Dixneuf, S.: Long optical cavities for open-path monitoring of atmospheric trace gases and aerosol extinction, *Appl. Opt.*, 48, B159–B171, doi:10.1364/AO.48.00B159, 2009.
- Varma, R. M., Ball, S. M., Brauers, T., Dorn, H.-P., Häseler, R., Heitmann, U., Jones, R. L., Meinen, J., Platt, U., Pöhler, D., Ruth, A. A., Shillings, J. E., Thieser, J., and Venables, D. S.: Aerosol extinction measurements using optical cavity spectrometers: an intercomparison of three broadband instruments, in preparation, 2012.
- 1435 Venables, D. S., Gherman, T., Orphal, J., Wenger, J. C., and Ruth, A. A.: High sensitivity in situ monitoring of NO<sub>3</sub> in an atmospheric simulation chamber using incoherent broadband cavity-enhanced absorption spectroscopy, *Environ. Sci. Technol.*, 40, 6758–6763, doi:10.1021/Es061076j, 2006.
- 1440 Vrekoussis, M., Kanakidou, M., Mihalopoulos, N., Crutzen, P. J., Lelieveld, J., Perner, D., Berresheim, H., and Baboukas, E.: Role of the NO<sub>3</sub> radicals in oxidation processes in the eastern Mediterranean troposphere during the MINOS campaign, *Atmos. Chem. Phys.*, 4, 169–182, 2004.
- Vrekoussis, M., Mihalopoulos, N., Gerasopoulos, E., Kanakidou, M., Crutzen, P. J., and Lelieveld, J.: Two-years of NO<sub>3</sub> radical observations in the boundary layer over the Eastern Mediterranean, *Atmos. Chem. Phys.*, 7, 315–327, 2007.
- 1445 Wängberg, I., Barnes, I., and Becker, K. H.: Product and mechanistic study of the reaction of NO<sub>3</sub> radicals with alpha-pinene, *Environ. Sci. Technol.*, 31, 2130–2135, 1997.
- Wayne, R. P., Barnes, I., Biggs, P., Burrows, J. P., Canosamas, C. E., Hjorth, J., Lebras, G., Moortgat, G. K., Perner, D., Poulet, G., Restelli, G., and Sidebottom, H.: *The Nitrate Radical - Physics, Chemistry, and the Atmosphere*, *Atmos. Environ.*, 25, 1–203, 1991.
- 1450 Wegener, R., Brauers, T., Koppmann, R., Rodriguez Bares, S., Rohrer, F., Tillmann, R., Wahner, A., Hansel, A., and Wisthaler, A.: Simulation chamber investigation of the reactions of ozone with short-chained alkenes, *J. Geophys. Res.*, 112, 1–17, doi:10.1029/2006JD007531, 2007.
- Wood, E. C., Wooldridge, P. J., Freese, J. H., Albrecht, T., and Cohen, R. C.: Prototype for in situ detection of atmospheric NO<sub>3</sub> and N<sub>2</sub>O<sub>5</sub> via laser-induced fluorescence, *Environ. Sci. Technol.*, 37, 5732–5738, doi: 10.1021/es034507w, 2003.
- 1455 Yokelson, R. J., Burkholder, J. B., Fox, R. W., Talukdar, R. K., and Ravishankara, A. R.: Temperature-Dependence of the NO<sub>3</sub> Absorption-Spectrum, *J. Phys. Chem.*, 98, 13 144–13 150, doi:10.1021/j100101a009, 1994.

**Table 1.** List of experiments performed during NO3Comp. The mixing ratios of key constituents are maximum values measured during the experiments. Ambient and dew point temperature ranges are given as well as the experiments' scopes.

Date	NO <sub>2</sub> ppbv	O <sub>3</sub> ppbv	NO <sub>3</sub> pptv	N <sub>2</sub> O <sub>5</sub> pptv	HNO <sub>3</sub> ppbv	<i>T</i> <sub>amb</sub> °C	<i>T</i> <sub>dew</sub> °C	Experiment
09 June	4	120	130	350	<sup>a</sup>	20.2–22.6	-43.6...-38.5	Stepwise change of NO <sub>2</sub>
10 June	4	230	170	300	0.7	18.2–28.5	-42.3...+9.2	Stepwise change of humidity
11 June	17	100	150	750	1.2	23.9–31.5	+8.7...+15.3	Measurements in ambient air including aerosol
12 June	8	200	400	1600	<sup>a</sup>	17.3–20.2	-57.2...-48.7	Short photolysis events
13 June	18	200	700	2200	4	18.2–29.5	-45.5...-43.7	Short photolysis events
14 June	12	135	180	850	6	19.3–28.1	-61.1...-47.7	Oxidation of butanal (max. 4 ppbv)
15 June	10	180	120	550	2	18.7–24.2	-58.9...+15.1	Addition of inorganic aerosol ((NH <sub>4</sub> ) <sub>2</sub> SO <sub>4</sub> )
16 June	38	60	55	1300	1.3	16.2–23.2	-50.4...-44.6	Oxidation of limonene <sup>(1)</sup> (max. 10 ppbv) +CO (500 ppmv)
17 June	11	19	40	770	<sup>a</sup>	13.2–22.9	-44.5...-47.6	Experiment of 16 June continued
18 June	33	60	150	1400	4.5	18.3–27.7	-1.2...+9.2	Oxidation of isoprene <sup>(2)</sup> (max. 10 ppbv) +(NH <sub>4</sub> ) <sub>2</sub> SO <sub>4</sub> seed aerosol + CO (500 ppmv)
20 June	75	100	400	5300	8	20.8–28.7	-56.0...-46.3	Oxidation of β-pinene <sup>(3)</sup> (max. 20 ppbv)
21 June	70	165	110	6000	3	18.3–20.4	-61.5...+10.9	Oxidation of β-pinene <sup>(3)</sup> (max. 20 ppbv)

<sup>a</sup> no valid measurements <sup>(1)</sup> Fry et al. (2011) <sup>(2)</sup> Rollins et al. (2009) <sup>(3)</sup> Fry et al. (2009)

**Table 2.** (a) Mean  $\text{NO}_3$  mixing ratio (centre of the frequency distribution, Fig. 2) and the corresponding confidence interval  $\frac{2\sigma}{\sqrt{n}}$ . (b) Comparison of the mean of the errors of zero- $\text{NO}_3$  measurements ( $\langle\sigma\rangle$ ) with the precision calculated from the frequency distribution of zero data ( $1\sigma$ -width of the Gaussian distribution). All values are in pptv.

		FZJ	NOAA	UAF	ULEIC	UCC	UHD
		DOAS	CRDS	CRDS	BBCRDS	IBBCEAS	CEDOAS
(a)	Mean $\text{NO}_3$	2.1	0.2	-0.2	0.1	0.2	3.4
	$\frac{2\sigma}{\sqrt{n}}$	0.70	0.01	0.05	0.38	0.03	1.38
(b)	$\langle\sigma\rangle$	$9.4 \pm 7.4$	$0.4 \pm 0.2$	$1.3 \pm 1.0$	$0.9 \pm 0.7$	$0.9 \pm 0.6$	$3.7 \pm 1.9$
	$1\sigma$	8.5	0.5	1.9	1.7	0.9	5.6

**Table 3.** Results of the correlation and linear regression analysis of NO<sub>3</sub> measurements from all instruments versus NOAA-CRDS as reference on the basis of 3-min averages. (a) Measurements in the absence of aerosol (cf. Fig. 5), (b) in the presence of aerosol (cf. Fig. 6).  $n$ ... number of data pairs,  $r^2$ ... Pearson linear correlation coefficient,  $\chi^2/(n-2)$ ... reduced chi-squared. A value of  $\approx 1$  indicates that the scatter of the data around the regression line is well covered by the individual  $1\sigma$  measurement errors (precision) of both instruments. In case the scatter of the data is larger 'fitexy' fails to calculate the correct regression parameters and their errors. The bold face numbers indicate the slope and intercept for an appropriate regression model ('least normal squares', LNS). For details see text in Sect. 3.3.2.

	Instrument	$n$	$r^2$	intercept/pptv	slope	$\frac{\chi^2}{(n-2)}$
(a)	FZJ	542	0.978	$2.9 \pm 0.5$	$1.05 \pm 0.005$	2.7
				<b><math>1.0 \pm 0.5</math></b>	<b><math>1.05 \pm 0.006</math></b>	
	UAF	654	0.992	$-0.4 \pm 0.3$	$1.01 \pm 0.002$	2.2
				<b><math>-1.8 \pm 0.4</math></b>	<b><math>1.04 \pm 0.006</math></b>	
	MPI	154	0.984	$-2.1 \pm 0.6$	$1.08 \pm 0.004$	4.1
				<b><math>-0.3 \pm 1.3</math></b>	<b><math>1.06 \pm 0.011</math></b>	
	ULEIC	250	0.964	$-3.3 \pm 0.4$	$0.91 \pm 0.002$	12.6
<b><math>-17.7 \pm 2.5</math></b>				<b><math>1.07 \pm 0.021</math></b>		
UCC	698	0.956	$1.6 \pm 0.3$	$1.08 \pm 0.002$	53.7	
			<b><math>-4.2 \pm 0.9</math></b>	<b><math>1.18 \pm 0.015</math></b>		
UHD	246	0.955	$2.5 \pm 0.5$	$0.93 \pm 0.004$	4.6	
			<b><math>-4.5 \pm 1.6</math></b>	<b><math>0.98 \pm 0.016</math></b>		
(b)	FZJ	855	0.989	$4.8 \pm 0.3$	$1.00 \pm 0.002$	3.3
				<b><math>5.2 \pm 0.4</math></b>	<b><math>1.00 \pm 0.003</math></b>	
	UAF	856	0.994	$-0.5 \pm 0.1$	$0.87 \pm 0.001$	3.7
				<b><math>0.6 \pm 0.2</math></b>	<b><math>0.85 \pm 0.005</math></b>	
	MPI	242	0.991	$1.1 \pm 0.4$	$0.94 \pm 0.001$	7.5
				<b><math>2.3 \pm 0.3</math></b>	<b><math>0.93 \pm 0.002</math></b>	
	ULEIC	465	0.991	$1.2 \pm 0.2$	$0.92 \pm 0.001$	46.
<b><math>1.0 \pm 0.4</math></b>				<b><math>0.94 \pm 0.005</math></b>		
UCC	879	0.996	$0.9 \pm 0.1$	$1.23 \pm 0.001$	115.5	
			<b><math>-2.8 \pm 0.3</math></b>	<b><math>1.34 \pm 0.005</math></b>		
UHD	246	0.981	$3.5 \pm 0.5$	$0.93 \pm 0.003$	3.1	
			<b><math>6.1 \pm 1.3</math></b>	<b><math>0.92 \pm 0.005</math></b>		

**Table 4.** Results of the correlation and linear regression analysis of all instruments versus NOAA-CRDS for each experiment. Data are 3 min averages ( $q \dots$  quality parameter - see text, <sup>a</sup>...  $q < 10^{-4}$ )

Date	Inst.	n	$r^2$	intercept/pptv	slope	$\frac{\chi^2}{(n-2)}$	q	Date	Inst.	n	$r^2$	intercept/pptv	slope	$\frac{\chi^2}{(n-2)}$	q
09 June	UCC	89	0.994	-0.4 ± 0.3	1.04 ± 0.003	3.3	<sup>a</sup>	15 June	UCC	113	0.981	-1.1 ± 0.4	1.17 ± 0.007	2.1	<sup>a</sup>
09 June	UAF	87	0.993	-0.5 ± 0.4	1.01 ± 0.004	2.4	<sup>a</sup>	15 June	UAF	108	0.900	-3.0 ± 0.7	0.86 ± 0.011	3.9	<sup>a</sup>
09 June	FZJ	79	0.967	3.1 ± 2.8	0.94 ± 0.034	0.7	0.9809	15 June	FZJ	111	0.707	28.0 ± 1.7	0.92 ± 0.028	3.7	<sup>a</sup>
09 June	UHD	17	0.977	1.5 ± 1.5	0.98 ± 0.020	3.1	0.0001	15 June	ULEIC	100	0.932	-4.2 ± 0.5	1.05 ± 0.009	7.7	<sup>a</sup>
10 June	UCC	78	0.974	1.5 ± 0.7	1.36 ± 0.007	12.7	<sup>a</sup>	15 June	UHD	55	0.934	-7.4 ± 1.5	1.06 ± 0.025	2.4	<sup>a</sup>
10 June	UAF	92	0.994	0.4 ± 0.8	1.05 ± 0.009	0.8	0.9044	16 June	UCC	275	0.959	1.4 ± 0.0	1.17 ± 0.002	253.8	<sup>a</sup>
10 June	FZJ	73	0.930	18.2 ± 1.5	0.90 ± 0.016	4.1	<sup>a</sup>	16 June	UAF	265	0.965	-1.1 ± 0.1	0.91 ± 0.007	2.1	<sup>a</sup>
10 June	ULEIC	29	0.937	-2.3 ± 0.6	0.72 ± 0.008	9.5	<sup>a</sup>	16 June	FZJ	280	0.750	3.6 ± 0.5	1.02 ± 0.029	1.4	<sup>a</sup>
10 June	UHD	57	0.953	1.9 ± 1.4	0.87 ± 0.014	1.7	0.0009	16 June	ULEIC	76	0.660	0.4 ± 0.1	0.73 ± 0.006	72.1	<sup>a</sup>
11 June	UCC	124	0.996	2.3 ± 0.5	1.32 ± 0.004	7.9	<sup>a</sup>	16 June	UHD	69	0.590	5.0 ± 0.4	1.02 ± 0.036	5.2	<sup>a</sup>
11 June	UAF	121	0.997	0.3 ± 0.6	0.91 ± 0.005	0.9	0.8531	16 June	MPI	51	0.945	-2.8 ± 0.3	1.03 ± 0.015	5.2	<sup>a</sup>
11 June	FZJ	98	0.966	1.2 ± 1.1	1.03 ± 0.010	3.9	<sup>a</sup>	17 June	UCC	329	0.993	1.2 ± 0.0	1.12 ± 0.001	15.7	<sup>a</sup>
11 June	ULEIC	81	0.963	-6.2 ± 0.6	0.90 ± 0.005	8.9	<sup>a</sup>	17 June	UAF	172	0.995	-1.2 ± 0.1	1.12 ± 0.008	0.5	1.0000
11 June	UHD	38	0.540	1.3 ± 14.8	0.85 ± 0.158	0.1	1.0000	17 June	FZJ	326	0.796	-0.7 ± 0.7	1.14 ± 0.028	1.5	<sup>a</sup>
12 June	UCC	131	0.999	-0.8 ± 0.5	1.10 ± 0.002	1.1	0.1566	18 June	UCC	284	0.999	1.8 ± 0.1	1.06 ± 0.003	9.3	<sup>a</sup>
12 June	UAF	107	0.998	-2.3 ± 1.1	1.09 ± 0.009	0.3	1.0000	18 June	UAF	275	0.998	-0.9 ± 0.1	0.95 ± 0.006	0.3	1.0000
12 June	ULEIC	44	0.994	0.7 ± 0.8	0.97 ± 0.006	5.5	<sup>a</sup>	18 June	FZJ	284	0.925	1.9 ± 0.5	0.98 ± 0.015	1.1	0.0571
12 June	UHD	65	0.986	3.8 ± 0.9	0.92 ± 0.006	4.8	<sup>a</sup>	18 June	ULEIC	88	0.997	1.8 ± 0.2	1.02 ± 0.006	39.4	<sup>a</sup>
13 June	UCC	65	0.999	3.6 ± 1.5	1.31 ± 0.004	0.2	1.0000	20 June	UCC	127	0.991	1.7 ± 0.7	1.32 ± 0.002	26.5	<sup>a</sup>
13 June	UAF	63	0.998	-1.2 ± 2.0	1.08 ± 0.006	0.6	0.9979	20 June	UAF	120	0.983	5.4 ± 0.9	0.84 ± 0.003	9.9	<sup>a</sup>
13 June	FZJ	65	0.997	2.5 ± 1.8	1.05 ± 0.006	1.4	0.0178	20 June	FZJ	127	0.994	1.0 ± 1.3	1.01 ± 0.004	1.8	<sup>a</sup>
13 June	ULEIC	62	0.987	2.7 ± 1.7	0.99 ± 0.005	7.4	<sup>a</sup>	20 June	ULEIC	107	0.982	6.1 ± 0.5	0.91 ± 0.001	24.9	<sup>a</sup>
13 June	UHD	30	0.975	-7.7 ± 3.6	1.01 ± 0.011	6.2	<sup>a</sup>	20 June	UHD	66	0.994	4.6 ± 1.8	0.93 ± 0.006	1.6	0.0009
13 June	MPI	16	0.998	-0.8 ± 1.6	1.03 ± 0.011	0.2	0.9995	20 June	MPI	107	0.974	3.0 ± 0.6	0.93 ± 0.001	3.3	<sup>a</sup>
14 June	UCC	157	0.967	-0.5 ± 0.2	0.96 ± 0.001	17.3	<sup>a</sup>	21 June	UCC	92	0.998	0.1 ± 0.1	1.13 ± 0.002	7.6	<sup>a</sup>
14 June	UAF	145	0.993	1.4 ± 0.7	0.96 ± 0.005	1.0	0.6123	21 June	UAF	87	0.991	2.7 ± 0.5	0.86 ± 0.010	0.8	0.8849
14 June	FZJ	150	0.908	22.2 ± 1.5	0.90 ± 0.012	2.9	<sup>a</sup>	21 June	FZJ	91	0.966	-1.1 ± 1.0	1.00 ± 0.018	1.2	0.1528
14 June	ULEIC	128	0.987	-14.1 ± 0.7	0.99 ± 0.005	2.1	<sup>a</sup>	21 June	ULEIC	30	0.988	-0.8 ± 0.5	1.19 ± 0.013	4.2	<sup>a</sup>
14 June	UHD	85	0.954	7.3 ± 1.1	0.89 ± 0.009	5.1	<sup>a</sup>	21 June	UHD	30	0.914	-2.8 ± 1.7	1.15 ± 0.035	1.7	0.0131
14 June	MPI	138	0.979	-3.5 ± 0.8	1.09 ± 0.006	4.4	<sup>a</sup>	21 June	MPI	91	0.991	1.6 ± 0.2	0.97 ± 0.003	5.0	<sup>a</sup>

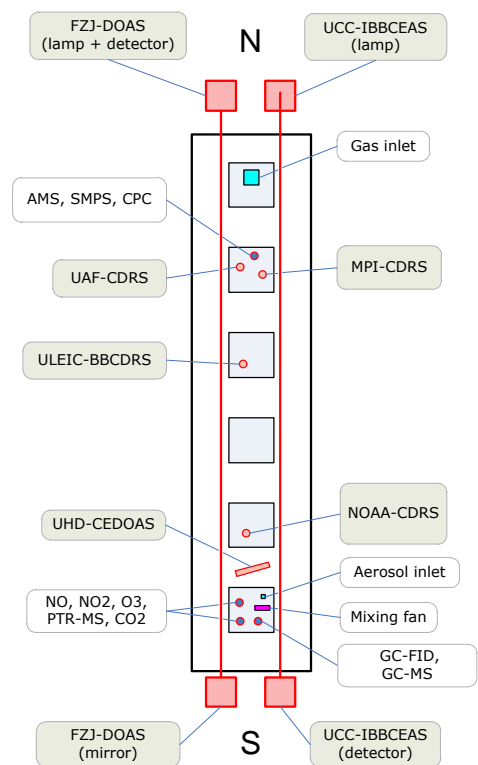


**Fig. 1.** Schematic top view onto the floor of SAPHIR with the positions of the individual instruments and inlet lines. The red lines indicate the open light paths of the FZJ-DOAS and UCC-IBBCEAS instruments, respectively. The UHD-CEDOAS open path instrument was assembled on the floor of the chamber. All other  $\text{NO}_3$  instruments drew air from flanges in the chamber floor at the designated positions.

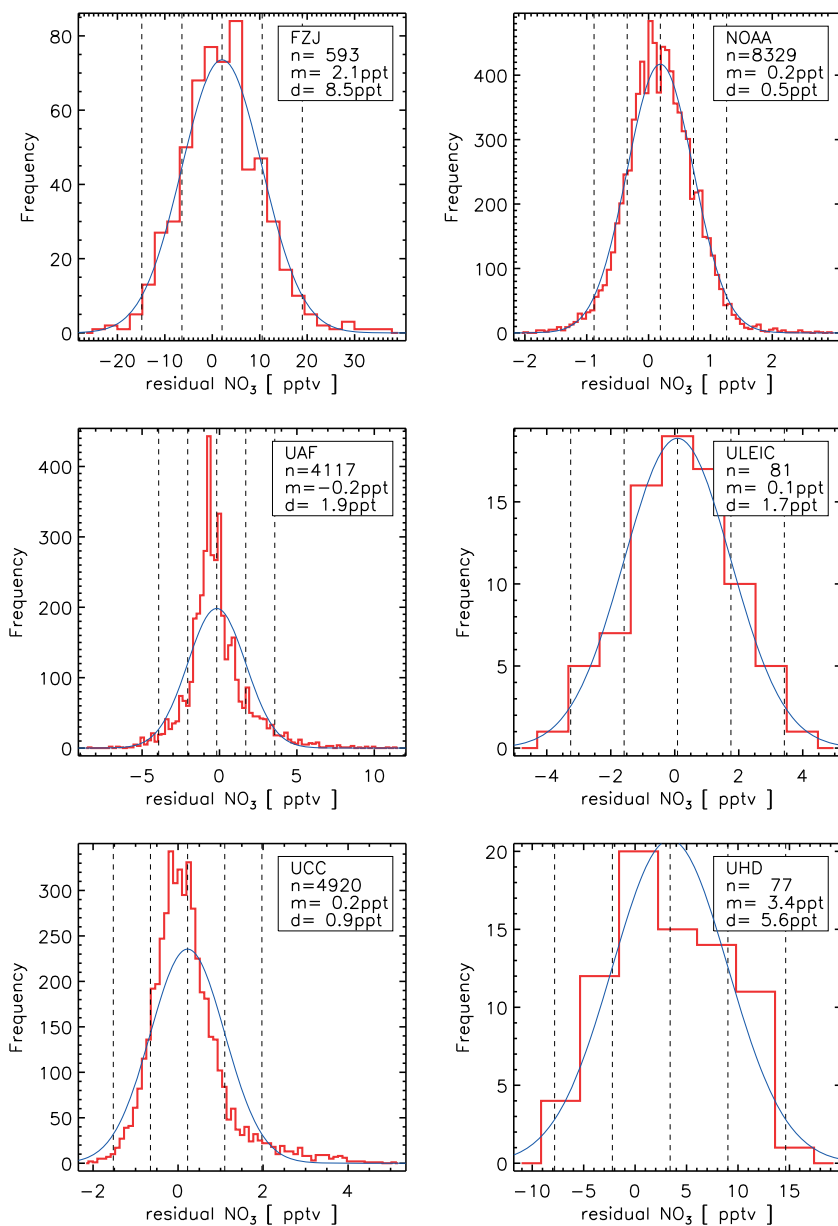


**Fig. 2.** Frequency distribution of zero-NO<sub>3</sub> mixing ratio measurements. A normal distribution (blue line) was fitted to the histograms. The histogram of the MPI-CRDS instrument is not shown because the number of available data points ( $n$ ) was too small to be statistically meaningful. The  $1\sigma$  standard deviation  $d$  is a measure for the instrumental precision during NO<sub>3</sub>Comp,  $m$  denotes the mean NO<sub>3</sub> mixing ratio.

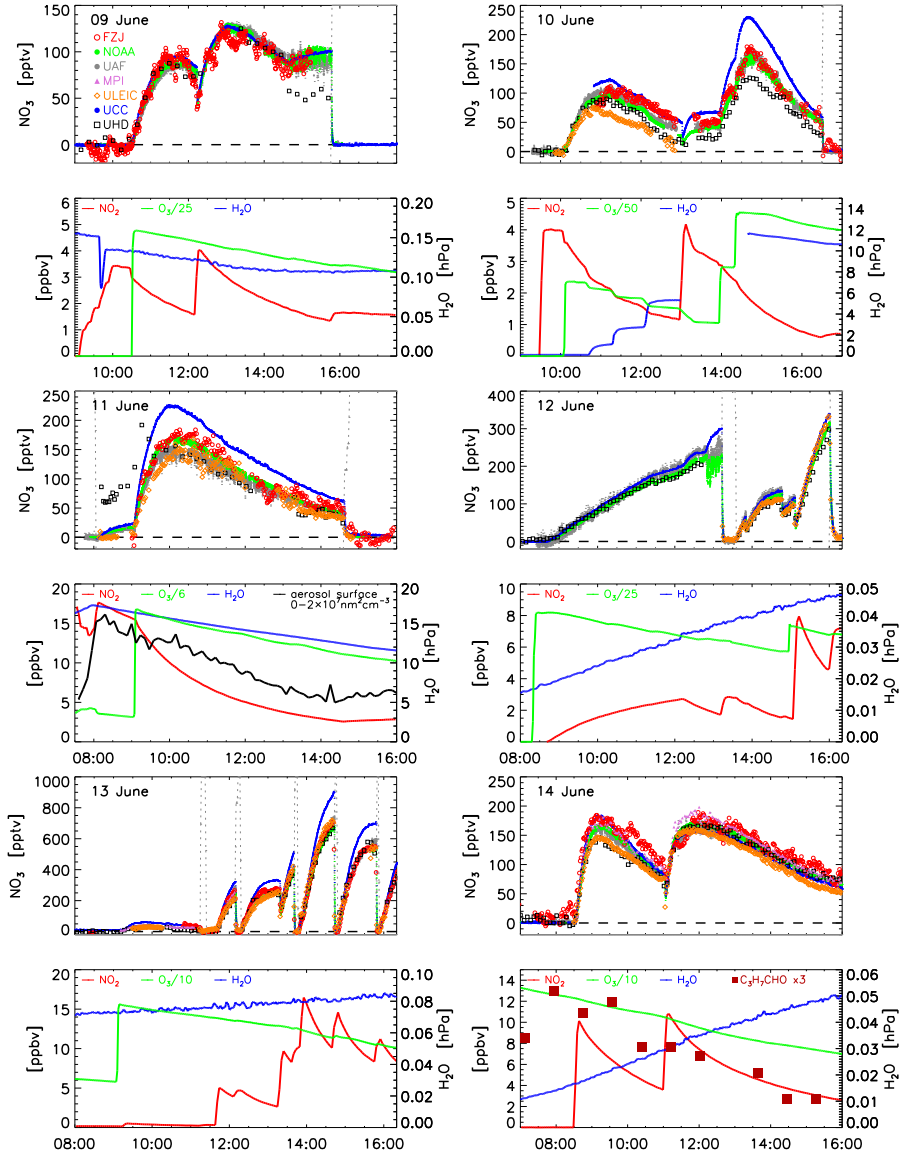


**Fig. 3.** Comparison of temporal profiles of  $\text{NO}_3$  mixing ratios and supporting measurements of other relevant species (as indicated in the panels) for all days of the intercomparison campaign. The respective upper panels show  $\text{NO}_3$  data measured with the original time resolution of the instruments (NOAA–CRDS 1 s, UAF–CRDS 1 s, UCC–IBBCEAS 5 s, MPI–CRDS 10 s, FZJ–DOAS 60 s, ULEIC–BBCRDS 61 s, and UHD–CEDOAS 300 s). Vertical, dashed grey lines indicate times when the roof of the chamber was opened or closed to initiate photolysis or enable the build-up of  $\text{NO}_3$ , respectively. The associated lower panels present the mixing ratios of  $\text{NO}_2$ ,  $\text{O}_3$ , hydrocarbons (ppbv, left axis), and the water vapour partial pressure (hPa, right axis). For experiments containing aerosol, the aerosol surface area concentration is indicated by a black line (in units of  $\text{nm}^2 \text{cm}^{-3}$ , no separate axis associated, full data span specified in the legend).

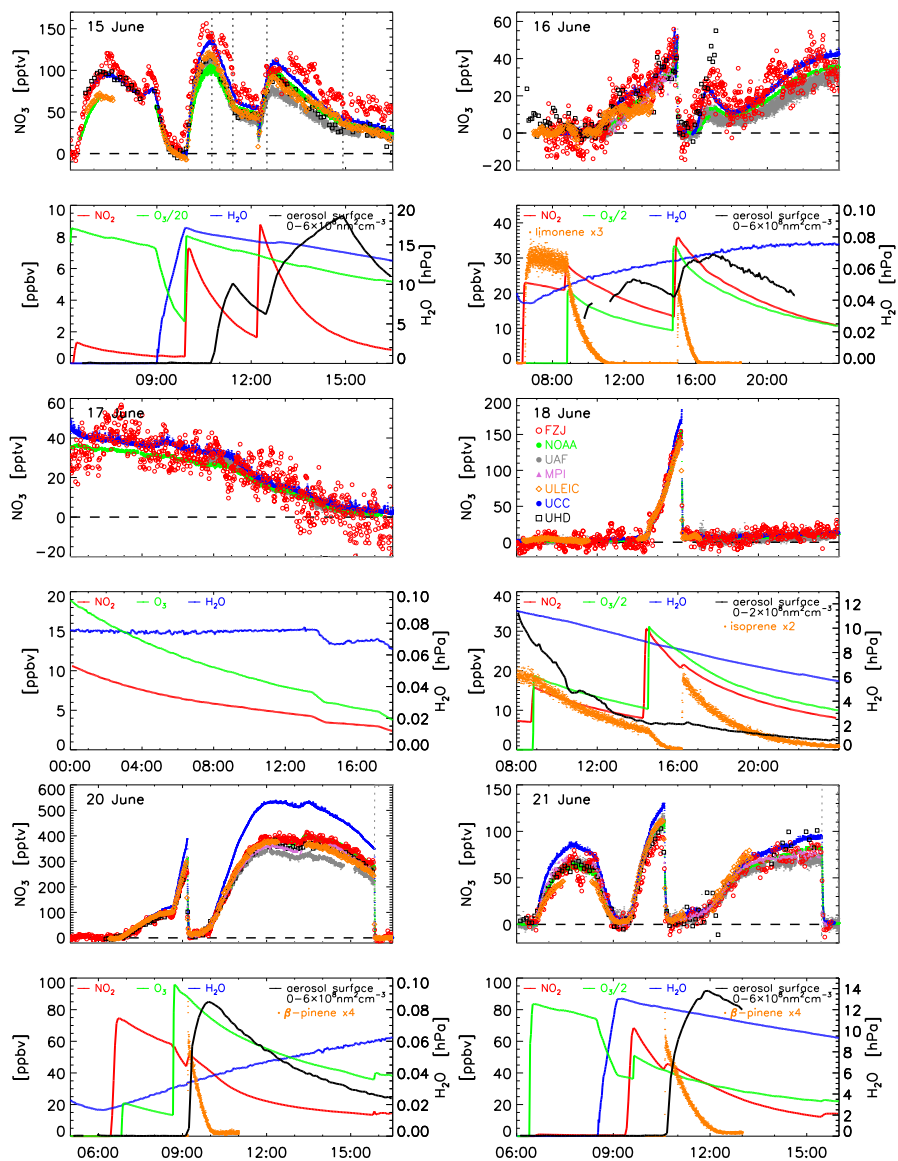


**Fig. 4.** Continued from Fig. 3. This figure comprises the chemically more complex experiments of the second part of the campaign. Dotted black lines on 15 June denote two time intervals during which inorganic aerosol was added to the chamber.

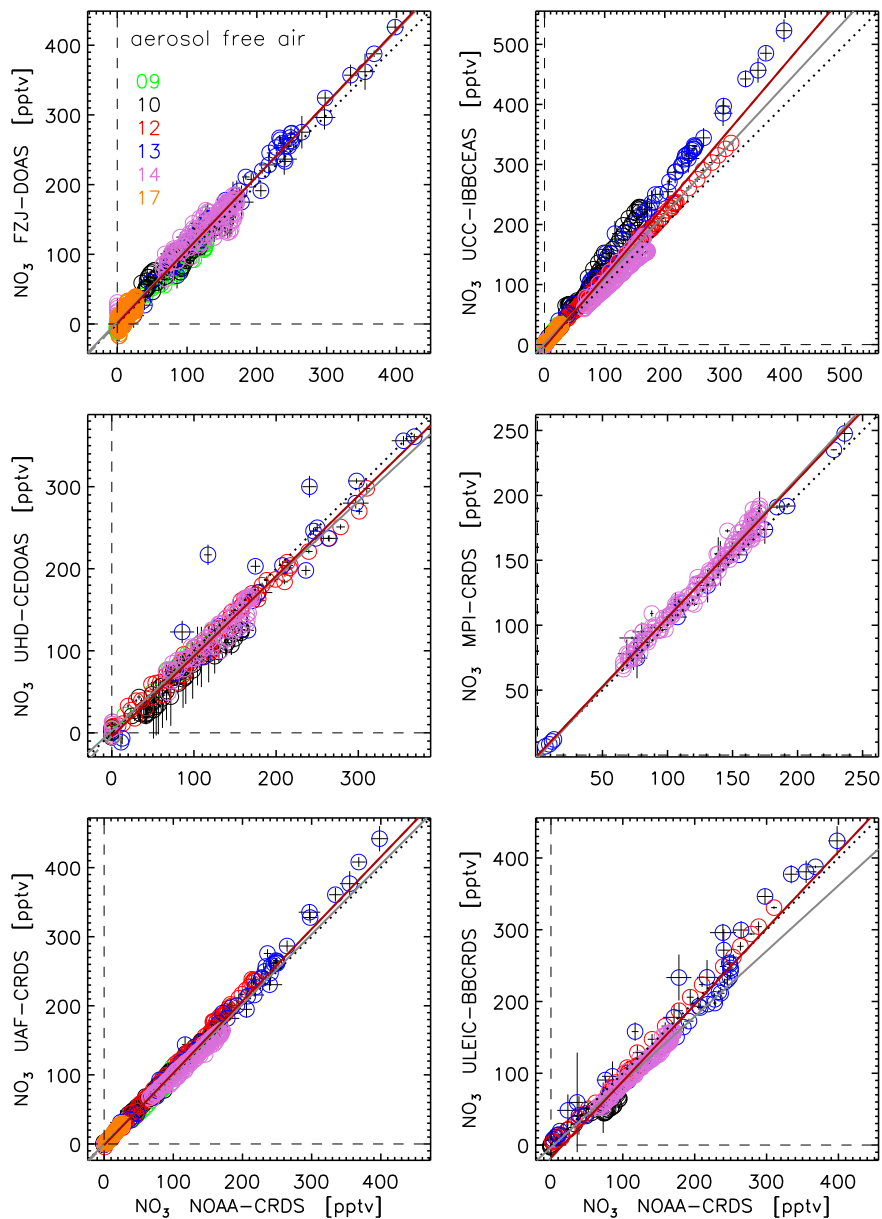


**Fig. 5.** Correlation of  $\text{NO}_3$  measurements versus the reference instrument NOAA-CRDS for aerosol free conditions. The data sets were averaged onto a common 3 min time grid and the data range was limited to 420 pptv to exclude any bias by the high mixing ratios of 13 June. The colour code denotes the experiment days and error bars are  $1\sigma$ . The 'best-fit' line (dark-red, solid line), calculated by a 'least-normal-squares' regression method, represents the average instrumental response for the entire intercomparison and the dotted black line shows the ideal 1:1 line. The solid grey lines are the linear regression lines calculated by the 'fitxy' algorithm. In case the scatter of the data is significantly larger than expected from the measurement errors the 'fitxy' algorithm fails to determine the correct relation between the data pairs (cf. Sect. 3.3.2 and Table 3).

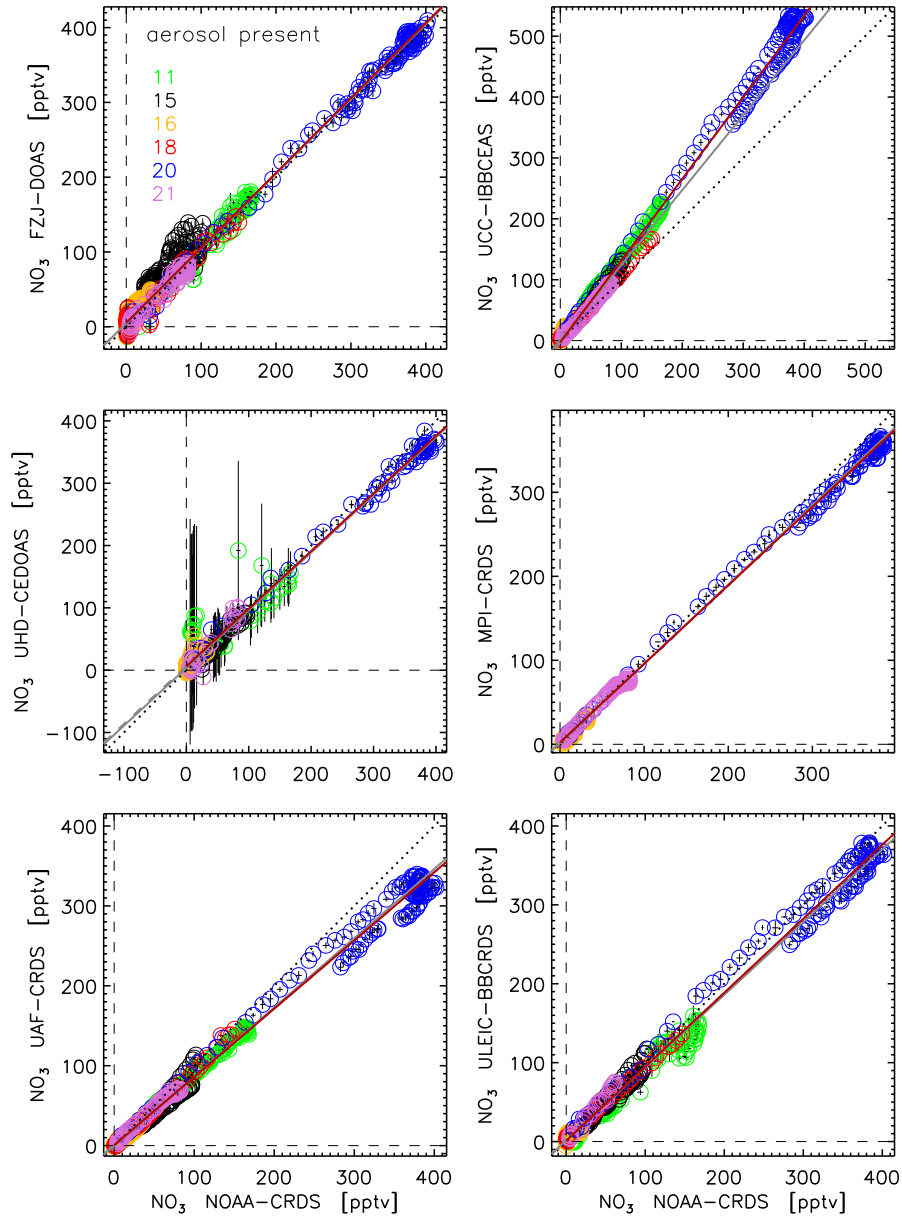


**Fig. 6.** Correlation of  $\text{NO}_3$  measurements versus the reference instrument NOAA-CRDS in presence of aerosol. See Fig. 5 for details on the regression lines.

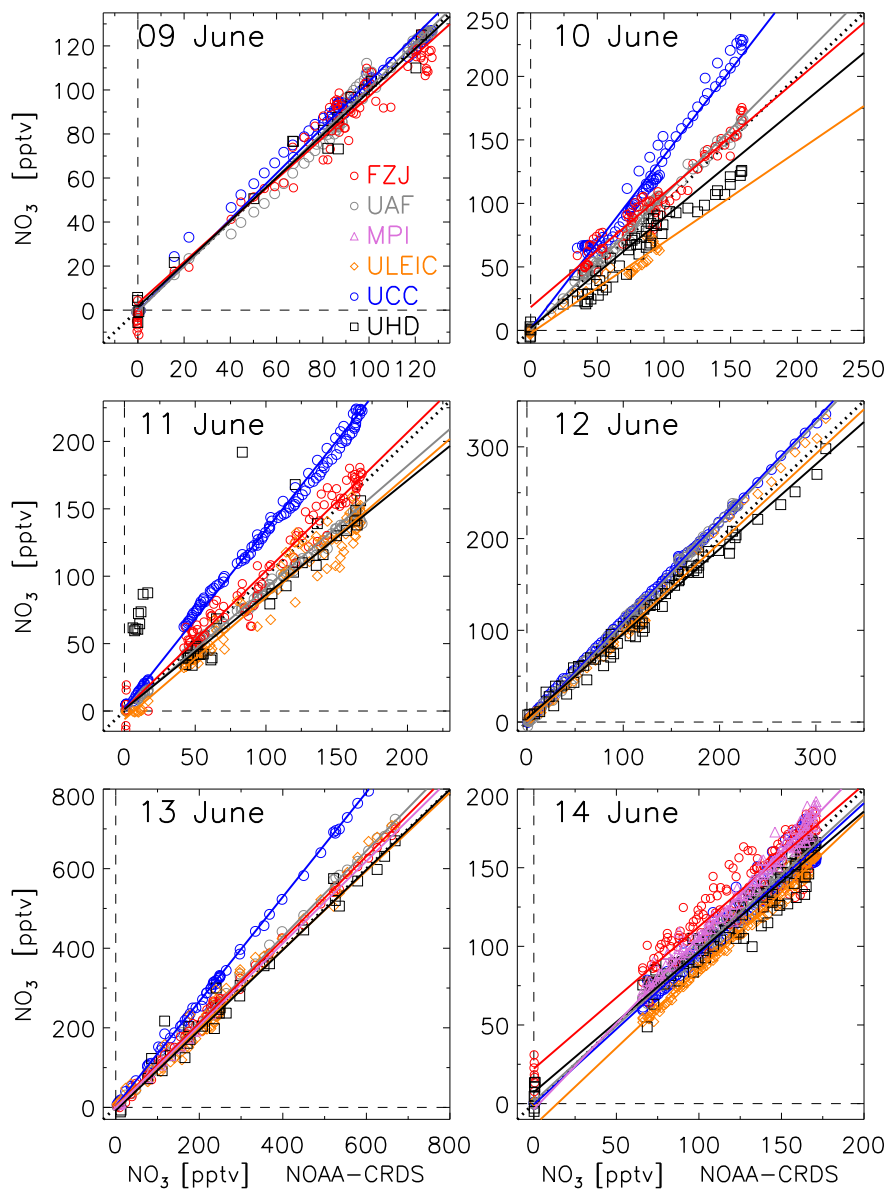


**Fig. 7.** Correlation and linear regression analysis for individual days of the intercomparison. The data sets were averaged to a common 3 min time grid. Linear regression lines calculated with the 'fitexy' algorithm are shown colour coded for the particular instruments. The dotted black line is the ideal 1:1 line. Error bars were omitted for clarity.

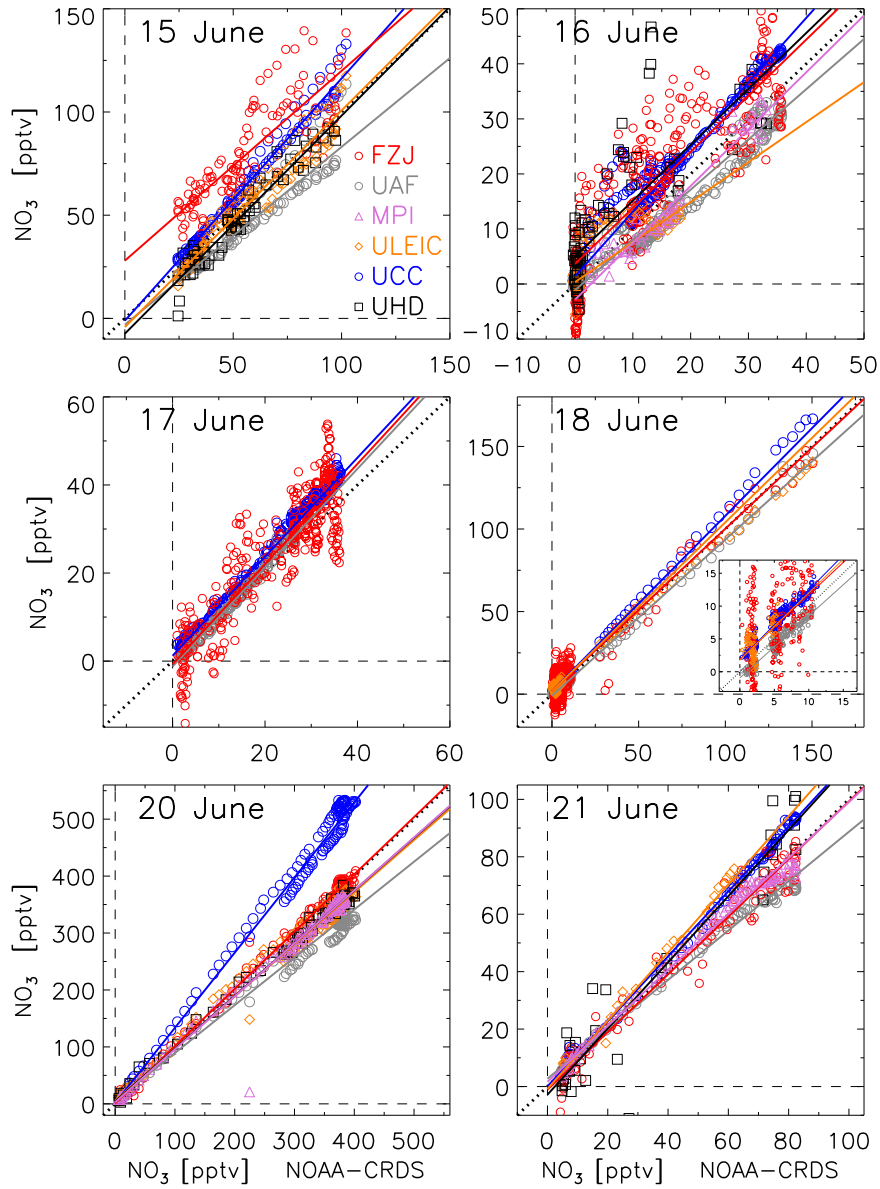


**Fig. 8.** Continued from Fig. 7. Inset on 18 June:  $\text{NO}_3$  mixing ratios in the presence of isoprene (08:00–14:00 UTC ( $\text{NO}_3 < 2$  pptv) and 16:10–24:00 UTC ( $\text{NO}_3 < 12$  pptv)).

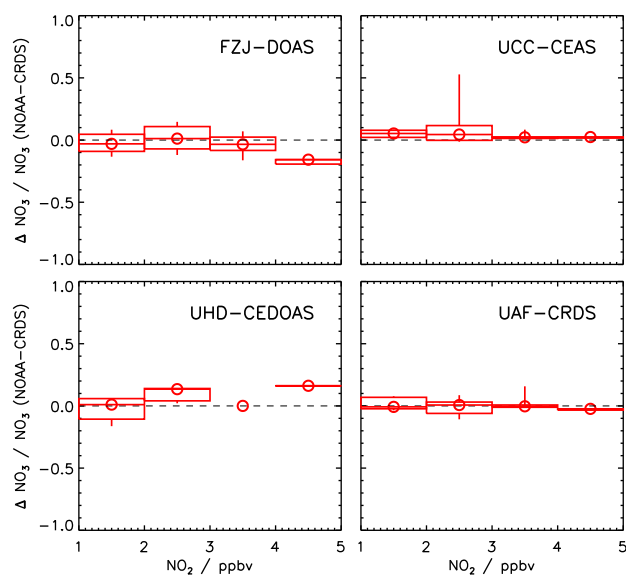


**Fig. 9.** Box and whisker plot of the relative difference of NO<sub>3</sub> measurements between various instruments and the reference NOAA-CRDS as function of the NO<sub>2</sub> mixing ratio during the chamber experiment on 9 June. Dots are medians, boxes give the first and third quartile and whiskers denote the 10th and 90th percentiles.

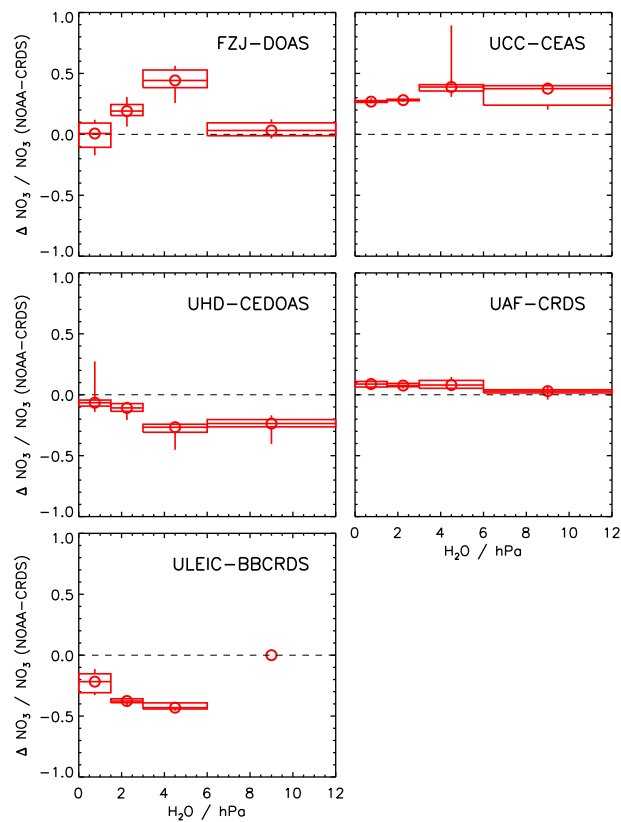


**Fig. 10.** Box and whisker plot of the relative difference of NO<sub>3</sub> measurements between various instruments and the reference NOAA-CRDS as function of the H<sub>2</sub>O partial pressure during the chamber experiment on 10 June. Dots are medians, boxes give the first and third quartile and whiskers denote the 10th and 90th percentiles.

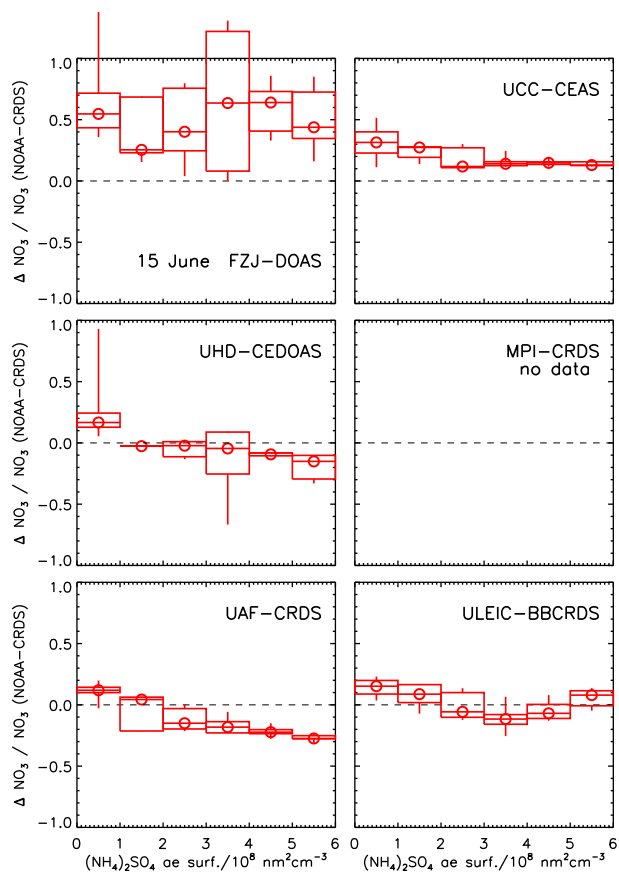


**Fig. 11.** Box and whisker plot of the relative difference of NO<sub>3</sub> measurements between various instruments and the reference NOAA-CRDS as function of the surface of ammonium sulfate aerosol during the 'inorganic aerosol' experiment on 15 June. Dots are medians, boxes give the first and third quartile and whiskers denote the 10th and 90th percentiles.

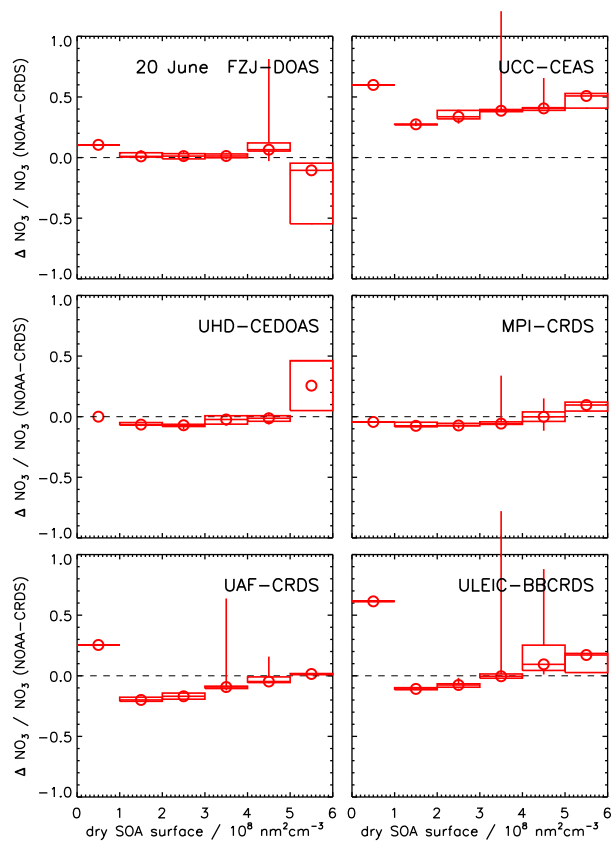


**Fig. 12.** Box and whisker plot of the relative difference of  $\text{NO}_3$  measurements between various instruments and the reference NOAA-CRDS as function of the surface of dry secondary organic aerosol (SOA) during the ' $\beta$ -pinene oxidation' experiment on 20 June. Dots are medians, boxes give the first and third quartile and whiskers denote the 10th and 90th percentiles.